


# FinDer v.2: Improved real-time ground-motion predictions for M2-M9 with seismic finite-fault characterization

## Journal Article

**Author(s):**

Böse, Maren; Smith, Deborah E.; Felizardo, Claude; Meier, Men-Andrien; Heaton, Thomas H.; [Clinton, John Francis](#) 

**Publication date:**

2018-01

**Permanent link:**

<https://doi.org/10.3929/ethz-b-000223418>

**Rights / license:**

[In Copyright - Non-Commercial Use Permitted](#)

**Originally published in:**

Geophysical Journal International 212(1), <https://doi.org/10.1093/gji/ggx430>

## FinDer v.2: Improved real-time ground-motion predictions for M2–M9 with seismic finite-source characterization

M. Böse,<sup>1</sup> D.E. Smith,<sup>2</sup> C. Felizardo,<sup>3</sup> M.-A. Meier,<sup>3</sup> T.H. Heaton<sup>3</sup> and J.F. Clinton<sup>1</sup>

<sup>1</sup>Swiss Seismological Service (SED), ETH Zurich, CH-8092 Zurich, Switzerland. E-mail: [mboese@sed.ethz.ch](mailto:mboese@sed.ethz.ch)

<sup>2</sup>US Geological Survey, Pasadena, CA 91106, USA

<sup>3</sup>California Institute of Technology, Pasadena, CA 91125, USA

Accepted 2017 October 6. Received 2017 August 28; in original form 2017 June 6

### SUMMARY

Recent studies suggest that small and large earthquakes nucleate similarly, and that they often have indistinguishable seismic waveform onsets. The characterization of earthquakes in real time, such as for earthquake early warning, therefore requires a flexible modeling approach that allows a small earthquake to become large as fault rupture evolves over time. Here, we present a modeling approach that generates a set of output parameters and uncertainty estimates that are consistent with both small/moderate ( $\leq M6.5$ ) and large earthquakes ( $> M6.5$ ) as is required for a robust parameter interpretation and shaking forecast. Our approach treats earthquakes over the entire range of magnitudes ( $> M2$ ) as finite line-source ruptures, with the dimensions of small earthquakes being very small ( $< 100$  m) and those of large earthquakes exceeding several tens to hundreds of kilometres in length. The extent of the assumed line source is estimated from the level and distribution of high-frequency peak acceleration amplitudes observed in a local seismic network. High-frequency motions are well suited for this approach, because they are mainly controlled by the distance to the rupturing fault. Observed ground-motion patterns are compared with theoretical templates modeled from empirical ground-motion prediction equations to determine the best line source and uncertainties. Our algorithm extends earlier work by Böse *et al.* for large finite-fault ruptures. This paper gives a detailed summary of the new algorithm and its offline performance for the 2016 M7.0 Kumamoto, Japan and 2014 M6.0 South Napa, California earthquakes, as well as its performance for about 100 real-time detected local earthquakes ( $2.2 \leq M \leq 5.1$ ) in California. For most events, both the rupture length and the strike are well constrained within a few seconds ( $< 10$  s) of the event origin. In large earthquakes, this could allow for providing warnings of up to several tens of seconds. The algorithm could also be useful for resolving fault plane ambiguities of focal mechanisms and identification of rupturing faults for earthquakes as small as M2.5.

**Key words:** Image processing; Spatial analysis; Earthquake early warning; Earthquake ground motions; Earthquake hazards; Earthquake source observations.

### INTRODUCTION

Earthquake early warning (EEW) systems must fulfill two tasks: to quickly identify potentially damaging earthquakes, and to provide accurate shaking predictions and robust warnings to end users, typically based on the exceedance of critical shaking levels (Böse *et al.* 2016a; Cauzzi *et al.* 2016a). With a few exceptions (e.g. Zollo *et al.* 2010; Hoshiaba & Aoki 2015), EEW processing typically consists of two steps: the first step is to determine the earthquake hypocentre and magnitude and the second step is to use these parameters in empirical ground-motion prediction equations (GMPEs) to predict the shaking that an end user will experience when located several tens of kilometres from the epicentre.

Speed is the most critical design target for EEW systems that respond to small to moderate-sized earthquakes ( $M \leq 6.5$ ), since the strongest shaking occurs mostly in small areas around the epicentre (e.g. Heaton 1985). In contrast, the accuracy of the shaking prognosis is most difficult in larger events ( $M > 6.5$ ), since (1) magnitudes calculated from seismic data tend to saturate (e.g. Bock *et al.* 2011; Melgar *et al.* 2015), and (2) finite-source dimensions must be known to predict future shaking, because this shaking is controlled by the rupture-to-site distance rather than by the hypocentral distance (e.g. Bommer & Akkar 2012; Böse *et al.* 2014).

While magnitude saturation in large earthquakes can be avoided by employing geodetic algorithms based on real-time positioning or displacement data (e.g. Yamada *et al.* 2007; Böse *et al.* 2013b;

Minson *et al.* 2014; Grapenthin *et al.* 2014a; Crowell *et al.* 2016), a fast detector is needed to provide real-time estimates of fault rupture dimensions. In Böse *et al.* (2012a), we propose a Finite-Fault Rupture Detector (FinDer) algorithm to characterize the fault rupture extent of an assumed line source for large earthquakes ( $M > 6.5$ ) based on the level and distribution of high-frequency acceleration peak amplitudes (PGA) observed in a seismic network. High-frequency motions are suitable for this purpose since, apart from the earthquake size, they are predominantly controlled by the rupture distance and are less affected by seismic slip and rupture directivity compared to mid- and long-period motions (Spudich & Chiou 2008).

Typically, EEW algorithms provide either point-source solutions, which are adequate to describe small-to-moderate-sized earthquakes ( $M < 6.5$ ), or finite-source models to characterize large fault ruptures ( $M > 6.5$ ). Point-source algorithms are either single sensor (e.g. Kanamori 2005; Wu *et al.* 2007; Böse *et al.* 2012b; Meier *et al.* 2015) or multiple sensor-based (e.g. Cua 2005; Allen 2007; Böse *et al.* 2008; Satriano *et al.* 2011; Kuyuk *et al.* 2014; Behr *et al.* 2015; Behr *et al.* 2016), and provide rapid estimates of earthquake magnitudes and hypocentres. Finite-source algorithms (e.g. Yamada *et al.* 2007; Böse *et al.* 2013b; Minson *et al.* 2014; Grapenthin *et al.* 2014a; Crowell *et al.* 2016), on the other hand, determine finite-fault models of large events, including, for instance, 2-D source dimensions and slip distributions. None of the current EEW algorithms is suited for application to both event classes. Recent studies (e.g. Meier *et al.* 2016), however, suggest that large finite-source earthquakes and smaller point-source events start similarly, implying that we can determine only lower bound magnitudes and must update source parameter estimates as long as fault rupture is occurring. This underlines the need for a consistent modeling approach that can be applied to both small earthquakes, which are typically modeled as point sources, and large earthquakes, which are typically modeled as finite-fault ruptures.

In this paper, we present a novel modeling approach that provides robust and improved real-time ground-motion predictions for point source as well as large finite-fault earthquakes. Our algorithm, called FinDer version 2 (v.2), extends earlier work of Böse *et al.* (2012a). While the original algorithm, however, can be applied only to large earthquakes ( $M > 6$ ), FinDer v.2 is suitable for application to the entire spectrum of earthquake sizes (M2–M9). Above all, the new algorithm allows for the detection of an earthquake that starts as a small (point source) event and then gradually develops into a greater magnitude earthquake.

## ALGORITHM

FinDer (and FinDer v.2) uses 2-D spatial template matching (e.g. Gonzales *et al.* 2004) to find the best line-source model to explain the observed ground-motion pattern in a seismic network at a given time. The algorithm compares an *image*  $I$  that represents the so far observed spatial distribution of peak absolute ground acceleration amplitudes with theoretical *templates*  $T$ , which are modeled from empirical GMPEs for line sources of different lengths; templates are rotated to determine the rupture strike. The line-source approximation is most appropriate for the case of a vertically dipping fault. For faults with smaller dips, the FinDer line source will usually translate in the fault perpendicular direction by several kilometres to reach a better match with the observed ground-motion pattern (see Discussion section).

FinDer minimizes iteratively the misfit between the  $T$  and  $I$  to recover the best  $T$  and its position in  $I$ , and thus determines the centroid  $X = \{\text{latitude, longitude}\}$ , length  $L$  and strike  $\theta$  of the corresponding line source. The earthquake magnitude  $M$  is estimated from empirical rupture-length-to-magnitude relations (e.g. Wells & Coppersmith 1994); the event origin time,  $t_0$ , is determined from the arrival times of peak amplitudes at various sensors.

The image  $I$  is created from the spatially interpolated logarithmic values of PGA observed in a seismic network at a given time; interpolation is done via Delaunay triangulation. PGA is determined at each station from the maximum absolute amplitude, which is taken over all three sensor components and over a configurable time window. Here, we choose a time window length of 120 s, corresponding to the approximate shaking duration of an M7.8 earthquake; if ground motions are still increasing, the time window is automatically extended during an earthquake. Any specific value,  $I(x, y)$ , results from the projection of the interpolated PGA amplitudes onto a Cartesian grid of height  $H$ , width  $W$ , and elements specified by coordinates  $(x, y)$ . In this study, we use a grid of  $5 \times 5$  km spatial resolution. The size of  $I$  is determined by the spatial extent of the seismic network to which FinDer is applied, plus some boundary which we set here as  $1^\circ$ . Site corrections can be applied, but they are of secondary importance here, because our approach takes into account ground motions at different stations deployed over large areas that usually encompass different site conditions (see Discussion section).

We model each value in our template,  $T(x, y)$ , from empirical GMPEs. For the examples shown in this paper, we use PGA relations of Cua & Heaton (2009) in combination with magnitude-rupture length relations of Wells & Coppersmith (1994). We compute our templates as

$$T(x, y) = \log_{10}(\text{PGA}(x, y)) = \left[ 0.73 M - 7.2 \right. \\ \left. \times 10^{-4} \left( \sqrt{R^2 + 9} + C(M) \right) \right. \\ \left. - 1.48 \log_{10} \left( \sqrt{R^2 + 9} + C(M) \right) - 0.42 \right] \\ + \log_{10}(1.1) \quad (1)$$

with  $C(M) = 1.16 \exp[0.96(M - 5)] \times [\arctan(M - 5) + \pi/2]$ , where PGA is given in  $\text{cm s}^{-1} \text{ s}^{-1}$  and distance  $R$  in km;  $R$  is the epicentral distance for  $M < 5$  and fault distance for  $M \geq 5$  to the assumed line source located in the centre of each template. The length  $L$  [km] of this line source is modeled as (strike-slip rupture, Wells & Coppersmith 1994)

$$\log_{10}(L) = (M - 4.33) / 1.49 \quad (2)$$

The factor  $\log_{10}(1.1)$  in eq. (1) is used to convert PGA from the root mean square of amplitudes to the maximum of each horizontal component ( $\max(E, N)$ ) as is used in FinDer (follows table 5.1 in Cua & Heaton 2009). We set the width  $w$  and height  $h$  of the templates as  $w = h = \min [145 (30 + 70 \log_{10}(L + 1))]$ , that is the template size grows logarithmically with rupture length  $L$  and linearly with magnitude  $M$ .

Our algorithm is independent of a particular set of relationships (in particular, the GMPEs and rupture length-to-magnitude conversion), and templates can be easily replaced, for example, to enable application to subduction-zone environments (Böse *et al.* 2015). The FinDer output depends on the GMPE selected for template generation. We have tested FinDer in different regions around the world, and we prefer the use of local relations whenever available. The template set is created externally and loaded by FinDer at

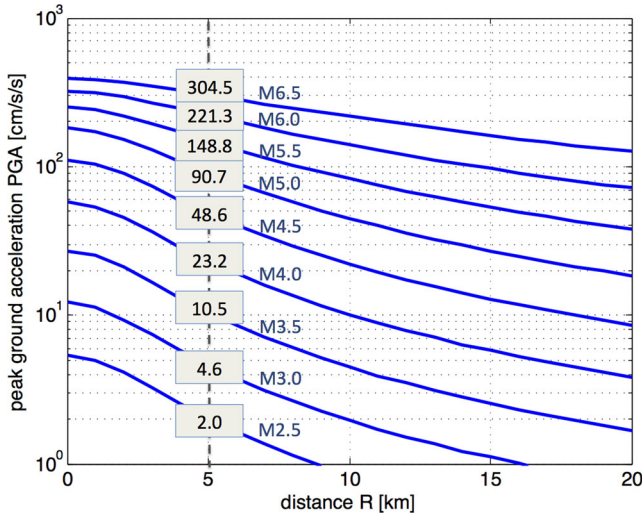


**Figure 1.** Ground-motion prediction equations for peak ground acceleration (PGA) after Cua & Heaton (2009) assuming rock condition. We use these relations in this paper to generate templates for FinDer. Ground-motion thresholds for binary template matching are determined at  $R = 5$  km distance, corresponding to our current template resolution, as  $\text{PGA}_{\text{threshold}} = \{2.0, 4.6, 10.5, 23.2, 48.6, 90.7, 148.8, 221.3, 304.5\}$  [ $\text{cm s}^{-1} \text{s}^{-1}$ ].  $R$  is the epicentral distance for magnitude  $M < 5$  and fault rupture distance for  $M \geq 5$ .

startup. The PGA relationships of Cua & Heaton (2009) are not hard-coded, but as our experience shows, they tend to agree well with the observed PGA amplitudes in our test regions, and we thus use them here as an example.

With the above approach we create a set of 56 templates for M2.5–M8.0, corresponding to rupture lengths of  $L = 0.06$ – $300$  km. The strike of each line-source is set as  $\Theta = 0^\circ$ , but during template matching we allow the templates to be rotated about the template centre up to  $180^\circ$  to determine the rupture strike. Note that the templates are symmetric around their line source, so that solutions at  $\Theta$  and  $\Theta + 180^\circ$  are equivalent.

In previous studies (Böse *et al.* 2012a, 2015), we found that *binary* template matching is more robust for PGA distributions compared to the continuous matching. Therefore, for a given list of ground-motion thresholds  $\text{PGA}_{\text{threshold}}$ , we define our binary images and templates as

$$I_{\text{threshold}}(x, y) = \begin{cases} 1 & \text{if } I(x, y) \geq \text{PGA}_{\text{threshold}} \\ 0 & \text{otherwise} \end{cases} \quad (3a)$$

and

$$T_{\text{threshold}}(x, y) = \begin{cases} 1 & \text{if } T(x, y) \geq \text{PGA}_{\text{threshold}} \\ 0 & \text{otherwise} \end{cases} \quad (3b)$$

In this study, we use  $\text{PGA}_{\text{threshold}} = \{2.0, 4.6, 10.5, 23.2, 48.6, 90.7, 148.8, 221.3, 304.5\}$  [ $\text{cm s}^{-1} \text{s}^{-1}$ ] corresponding to the average peak acceleration generated by earthquakes of  $2.5 \leq M \leq 6.5$  (increase with half-magnitude unit) at  $R = 5$  km distance (Fig. 1) as determined from eq. (1). Using a list of PGA thresholds is needed to extend FinDer to the entire range of earthquake magnitudes. This is a major change from our original algorithm described in Böse *et al.* (2012a 2015), in which a single large threshold (usually  $70 \text{ cm s}^{-1} \text{s}^{-1}$ ) was used, and thus only large earthquakes ( $M > 6.0$ ) could be processed.

Ground-motion distributions in small and moderate earthquakes are usually of a radial-symmetric shape around the epicentre, whereas in the case of larger events ( $>M6.5$ ), they are usually quasi-elliptic around the rupturing fault. Selecting a ground-

motion threshold for the larger earthquakes is less critical, since the templates mainly describe the shape of shaking distributions, which is controlled by length  $L$  (and thus magnitude  $M$ ), and less affected by the image resolution (here 5 km). We could in principle extend our list to larger ground-motion thresholds. However, these values are not required, but mainly increase the computation time, since more parameters (ground-motion thresholds) must be tested, slowing down real-time performance.

We define each  $(x, y)$  position element of the *result matrix*,  $R$ , for a given  $(L, \Theta)$  as

$$R(x, y|L, \Theta) = \frac{\sum_{x', y'} [T_{\text{threshold}}(x', y'|L, \Theta) - I_{\text{threshold}}(x+x', y+y')]^2}{\sqrt{\sum_{x', y'} T_{\text{threshold}}(x', y'|L, \Theta)^2 \cdot \sum_{x', y'} I_{\text{threshold}}(x+x', y+y')^2}} \quad (4)$$

where values of  $R(x, y|L, \Theta)$  can vary from 0 to 1. The result matrix contains the normalized misfit values for different template positions, as it overlaps the image matrix (for a given length and strike). Eq. (4) slides through  $I$  and compares the patches of size  $w \times h$ , in which  $I$  and  $T$  overlap. The summation is done over the patch  $x' = 0 \dots w - 1$ ,  $y' = 0 \dots h - 1$ . Generally, the spatial coverage of  $I$  is much larger than that of  $T$ , where the height and width of  $R$  are defined as  $H_R = (H - h + 1)$  and  $W_R = (W - w + 1)$ , respectively. Ultimately, we are interested in the template position with the minimum normalized misfit value in  $R$ , which we define as  $E$ . The centre point of the corresponding template yields an estimate of the rupture centroid position.

Since a complete search over all templates (and thus over all rupture lengths  $L$  and magnitudes  $M$ ), rotation angles (strike)  $\Theta$ , and thresholds  $\text{PGA}_{\text{threshold}}$  is too time-consuming for real-time application, we shrink our search space as follows (see Fig. 2): for each  $\text{PGA}_{\text{threshold}}$ , we calculate an initial estimate of rupture length,  $L$ , then apply the divide-and-conquer algorithm (e.g. Cormen *et al.* 2009) to estimate the best strike  $\Theta$  for different rupture lengths  $L$  about our initial guess. We continue this search until a  $\Theta/L$  combination is found that minimizes  $E$ . In detail, we generate our initial estimate of length  $L$  by calculating the number of pixels above  $\text{PGA}_{\text{threshold}}$  for both the image,  $I$ , and for all the templates,  $T$ ; we consider only  $\text{PGA}_{\text{threshold}}$  values for which a minimum number of pixels is exceeded (e.g. 10 pixels). The initial estimate of  $L$  (for a given  $\text{PGA}_{\text{threshold}}$ ) is obtained by selecting the template (with an associated  $L$ ) whose number of pixels above  $\text{PGA}_{\text{threshold}}$  best matches the observed number of pixels above  $\text{PGA}_{\text{threshold}}$  in the image. Starting from this initial guess, we apply the divide-and-conquer algorithm over  $\Theta$ : we divide the angular space, calculate the misfit  $E$  for each  $\Theta$ , determine which strike interval has the smallest  $E$ , subdivide this interval, calculate  $E$  again for each  $\Theta$  (in this interval), and repeat this procedure until we reach the specified angular resolution. We first apply this divide-and-conquer algorithm to the strikes associated with our initial rupture length  $L$ , and then search the two closest rupture lengths around this initial  $L$  (applying divide-and-conquer to the strikes) to determine the  $\Theta/L$  combination that best minimizes  $E$ . The iterative procedure is visualized in Fig. 2. Our misfit values as a function of rupture length,  $L$ , vary smoothly and have an absolute minimum that works nicely for finding the minimum  $E$ .

The same procedure is repeated for each  $\text{PGA}_{\text{threshold}}$  and the corresponding solutions of  $L$ ,  $\Theta$  and  $E$  are computed. The  $\text{PGA}_{\text{threshold}}$  value and corresponding parameter estimates with the smallest misfit are preferred and reported. The  $\text{PGA}_{\text{threshold}}$  value is stored for future event updates: once the processing has stepped into a

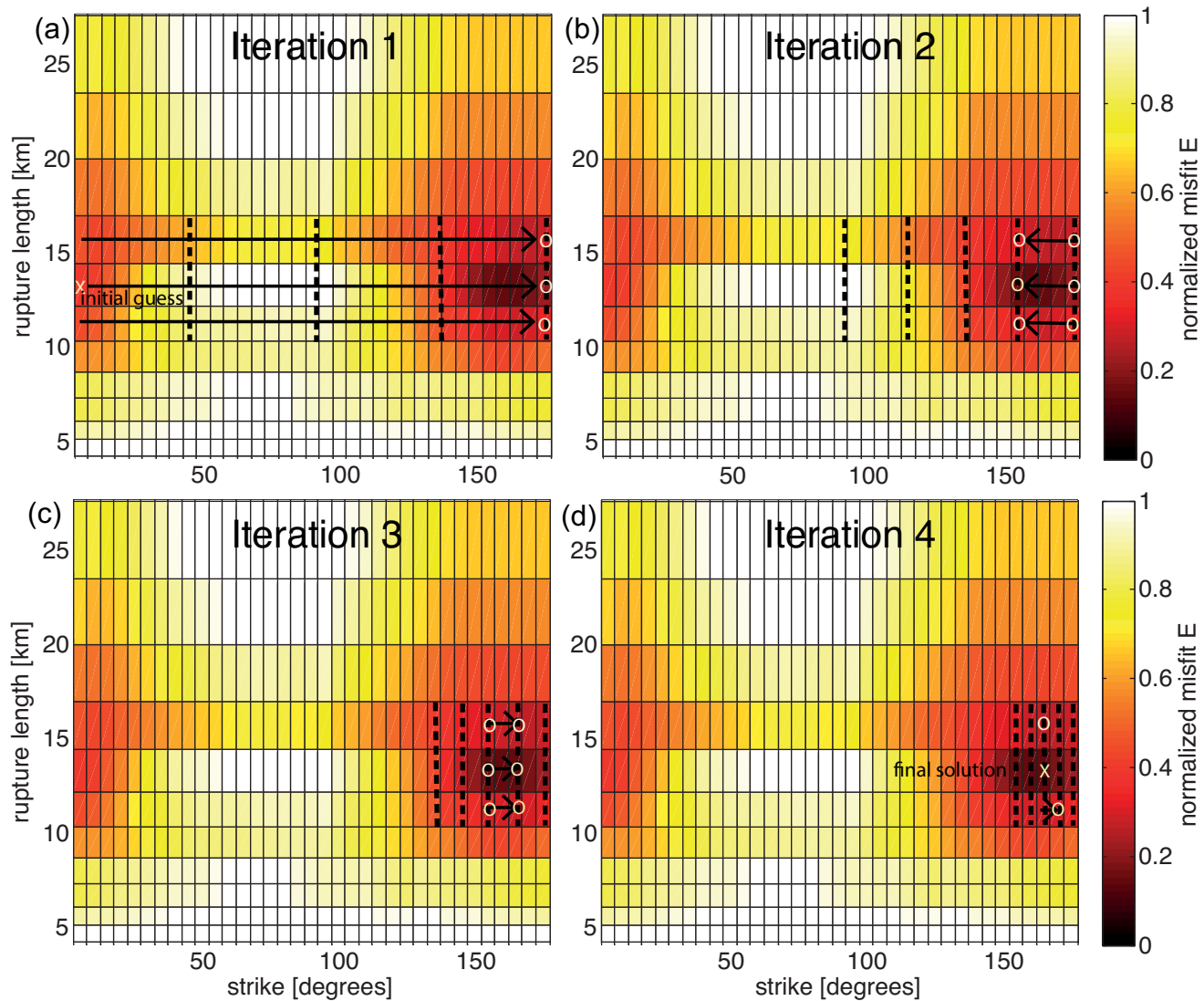


**Figure 2.** Iterative procedure to find the minimum normalized misfit,  $E(L, \Theta)$ , between the observed ground-motion *image*,  $I_{\text{threshold}}$ , and a set of modeled templates,  $T_{\text{threshold}}$ , to determine the best FinDer line-source model (characterized by rupture length,  $L$ , and strike,  $\Theta$ ) for a given PGA threshold,  $\text{PGA}_{\text{threshold}}$ .  $E$  is generally well behaved over rupture length with a clear single minimum, and we can hence search stepwise in the  $\pm$  directions along  $L$ ; however,  $E$  is cyclic and more complex with regards to  $\Theta$ , so we need to explicitly search over the entire strike space. We start from an initial guess of  $L$ , for which the number of pixels exceeding  $\text{PGA}_{\text{threshold}}$  in both the image and the template, that corresponds to this particular  $L$ , agree best [here  $L = 13.2$  km corresponding to M6.0, eq. (2), marked by ‘X’ in (a)]; we also consider the two neighbored lengths (here  $L = 11.3$  and  $15.4$  km, corresponding to M5.9 and M6.1, respectively). For each of the three rupture lengths, we determine  $\Theta$  by rotating the corresponding template and calculating the misfit. To avoid testing each possible strike from  $0^\circ$  to  $180^\circ$ , we apply the divide-and-conquer algorithm, which takes samples at increasing strike density. (a) shows the first divide-and-conquer sampling with dashed vertical lines. In this example, we take five strike samples for each of the three rupture lengths ( $L = 13.2, 11.3$  and  $15.4$  km). For each  $L$ , we then choose the strike sample with the smallest misfit (here  $\Theta = 180^\circ$ ), and resample in (b). The samples in (b) are taken by subdividing the two strike intervals encompassing our previous iteration in (a) (here from  $90^\circ$  to  $180^\circ$ ). Then based on these samples, we choose the best sample from the minimum misfit, and resample again in (c). This procedure is repeated again in (d). In general, we continue subdividing until the strike resolution is reached (here  $5^\circ$ ). In the example shown here, the best strike is found after four iterations. Finally, we compare the misfit for the best strike for each of the three rupture lengths, and end up with a final rupture length and strike estimate of  $L = 13.2$  km and  $\Theta = 160^\circ$ , shown by the white ‘X’ in (d). These parameters characterize the FinDer-determined line-source model.

higher  $\text{PGA}_{\text{threshold}}$ , it does not go backwards to a smaller threshold. Processing is continued at this (or a higher) threshold if the earthquake continues to increase, that is we only allow the earthquake to grow over time. For each line-source solution, we calculate also the misfit profile functions for  $L$  and  $\Theta$ , while keeping the centroid position fixed, and determine the marginal likelihood functions  $p(L|X, \Theta)$  and  $p(\Theta|X, L)$ . All estimates are updated regularly when a new set of PGA values becomes available. The FinDer template match-

ing approach is computationally highly efficient ( $<1$  s per source parameter update), so that large earthquake fault ruptures can be characterized while still in progress (Böse et al. 2015).

The FinDer v.2 algorithm is implemented in C++ and utilizes widely tested open-source libraries for geographic mapping (*The Generic Mapping Tools*—GMT; Wessel et al. 2013) and computer vision (*Open Source Computer Vision*—OpenCV; <http://opencv.org>). We employ the C/C++ GMT API for

interpolating 2-D scattered PGA data onto a regular Cartesian grid and the OpenCV libraries primarily for template matching. Additional GMT functions are used for plotting.

## RESULTS

In the following, we examine the performance of FinDer v.2 from playback of waveforms recorded during the 2016 M7.0 Kumamoto (Japan) and 2014 M6.0 South Napa (Northern California) earthquakes. We then analyse the performance of the algorithm in California during an 8-month test phase, in which FinDer v.2 ran in real time within the ANSS Quake Monitoring System (AQMS)/Earthworm framework of the California Integrated Seismic Network (CISN). For simplicity, we use in the following the generic name ‘FinDer’ to refer to the new FinDer v.2 algorithm.

### Example 1: 2016 M7.0 Kumamoto (Japan) earthquake

The M7.0 Kumamoto earthquake ( $M_{\text{JMA}} 7.3$ ,  $32.76^\circ\text{N}$ ,  $130.76^\circ\text{E}$ , 12 km; Japan Meteorological Agency, JMA) on 2016 April 15 16:25:06 UTC is one of the largest and most destructive crustal earthquakes that has occurred in Japan in recent years. It caused substantial losses, including 69 fatalities, 1747 casualties and more than 180 000 people needed evacuation (Goda *et al.* 2016). The main shock occurred along the active Futagawa strike-slip fault, with rupture propagating for approximately 30–50 km mainly towards the northeast direction (Yagi *et al.* 2016; Yano & Matsubara 2016). Waveform inversions and aftershock distributions suggest that the rupture terminated near the southwestern side of the Mt. Aso volcano, possibly due to the high-temperature area around the magma chamber (Yagi *et al.* 2016). In their  $W$ -phase moment tensor solution, the National Earthquake Information Center (NEIC) determines the rupture strike and dip of the Kumamoto main shock as  $224^\circ$  and  $66^\circ$ , respectively.

An isolated area of seismic activity at about 80 km northeast of the epicentre ( $33.28^\circ\text{N}$ ,  $131.35^\circ\text{E}$ , 5 km; Nakamura & Aoi 2017) is probably generated by a secondary event, possibly triggered by the main shock through external perturbations, such as stress changes (Nakamura and Aoi 2017). This second earthquake ( $\sim M_{\text{JMA}} 5.7$ ; Kodera *et al.* 2016) occurred about 32–34 s after the M7.0 Kumamoto earthquake; its waveforms are mostly hidden in the main shock coda, and the event is visible mainly in the high-frequency band (Hoshiya 2017).

The JMA EEW system (Hoshiya *et al.* 2008) issued a first public warning 8 s after the origin of the Kumamoto main shock, which was 3.9 s after the event was detected (Kodera *et al.* 2016). Although the initial magnitude was underestimated as  $M_{\text{JMA}} 5.9$  ( $\sim M 5.7$ , using updated relations by Oth *et al.* 2010; Oth, 2017, private communication), it was large enough to meet the criteria for issuing a warning. Five seconds later, the magnitude was upgraded to  $M_{\text{JMA}} 6.9$  (Kodera *et al.* 2016;  $\sim M 6.6$ ). Although the second  $M_{\text{JMA}} 5.7$  ( $\sim M 5.5$ ) event at 80 km distance did not affect the hypocentre and magnitude estimates for the main shock, the system underpredicted the seismic intensity (4 JMA scale) in the area around the secondary earthquake, which was observed as 6 L (Kodera *et al.* 2016).

In order to simulate the performance of FinDer v.2 for the Kumamoto main shock, we process in a real-time ‘playback’ simulation, the archived waveforms recorded at 220 KiK- and K-Net strong-motion stations of the National Research Institute for Earth Science and Disaster Resilience (NIED; Fig. 3). We neglect data communication and processing delays and update source param-

eter estimates every half a second. At 3.5 s of the event origin, the minimum ground-motion threshold of  $2 \text{ cm s}^{-1} \text{ s}^{-1}$  is exceeded at two stations (which is our current trigger criteria), and a first FinDer report is released (Fig. 3a). The magnitude is initially underestimated as  $M_{\text{FinDer}} 3.2$  ( $M_{\text{FinDer}}$  is an estimate of moment magnitude  $M$ ), but quickly updated (Figs 3b–f). At 8.5 s from the event origin, which coincides with the approximate time at which the first JMA warning was released ( $M_{\text{JMA}} 5.9$ ;  $\sim M 5.7$ ), the FinDer estimated magnitude is  $M_{\text{FinDer}} 6.6$ . The length and strike of the FinDer-determined line source at this time, indicated by a black line in Fig. 3, are estimated as  $L = 33 \text{ km}$  and  $\Theta = 215^\circ$ , respectively. The complete temporal evolution of FinDer length and strike estimates is shown in Figs 4(a) and (b).

For each FinDer-determined line-source model, which is updated every half second, we compute the rupture-to-site distances and predict from those the level and distribution of PGA from the Cua & Heaton (2009) relationships, which were also used for template generation. The resulting predicted PGA levels are shown in Fig. 3 as colour-coded contour lines. The up-to-date observed PGA values are represented by colour-coded symbols: we use squares, whenever the predicted PGA exceeds  $37 \text{ cm s}^{-1} \text{ s}^{-1}$  (corresponding to ‘moderate shaking’ on Modified Mercalli Intensity (MMI) scale) in any report given so far, otherwise we use inverted triangles. Beginning at  $\sim 8.5 \text{ s}$  from the event origin, FinDer predicts considerable shaking in large parts of Kyushu Island, in many cases before shaking at these sites is felt (Figs 3c–f). Similar to the JMA system, areas near the epicentre are within the blind zone of the EEW system and would not have received a warning before considerable shaking starts. More distant sites, however, that still experience very strong shaking in this event, could receive a warning of 20–40 s before moderate or large shaking occurs (Fig. 4c), even with realistic delays of 1–2 s.

The smaller M5.5 earthquake at about 16:25:38 UTC, which was likely triggered by the main shock (Kodera *et al.* 2016; Hoshiya 2017), causes a secondary patch of significant high-frequency shaking at about 80 km northeast of the M7.0 Kumamoto epicentre (Fig. 3f). As a result, FinDer moves its line source towards this patch to optimize the match between the observed and predicted ground motions. Although FinDer combines the two events into a single line-source model, the predicted and observed motions agree well and allow for a more precise shaking characterization compared to the point-source solution of the event. We note that the secondary smaller earthquake was not detected in real time by the JMA system, because it was hidden in the main shock coda and, as a consequence, shaking northwest of Oita was underestimated (Kodera *et al.* 2016; Hoshiya 2017).

The strike of the final FinDer line source is estimated at  $220^\circ$ , which differs by  $4^\circ$  compared to the NEIC and NIED moment tensor solutions (Figs 4d–e). The FinDer preferred rupture length of  $L = 84 \text{ km}$  ( $\sim M 7.2$ , eq. 2), however, is almost twice as long as reported in the literature (Yagi *et al.* 2016; Yano & Matsubara 2016). This extended rupture and the corresponding larger magnitude, however, are required to yield a better match with the observed PGA pattern caused by the Kumamoto main shock and its strong along-strike directivity, and subsequently also by the secondary smaller event at 80 km distance. A simple point-source model as shown in Fig. 4(f), here determined from PGA relations by Cua & Heaton (2009) for M7.0 and the correct hypocentre location assuming rock condition, clearly fails in reproducing the observed PGA values: ground motions are strongly underestimated for most regions on Kyushu Island, when source dimensions are neglected (Fig. 4c). This highlights one of the core

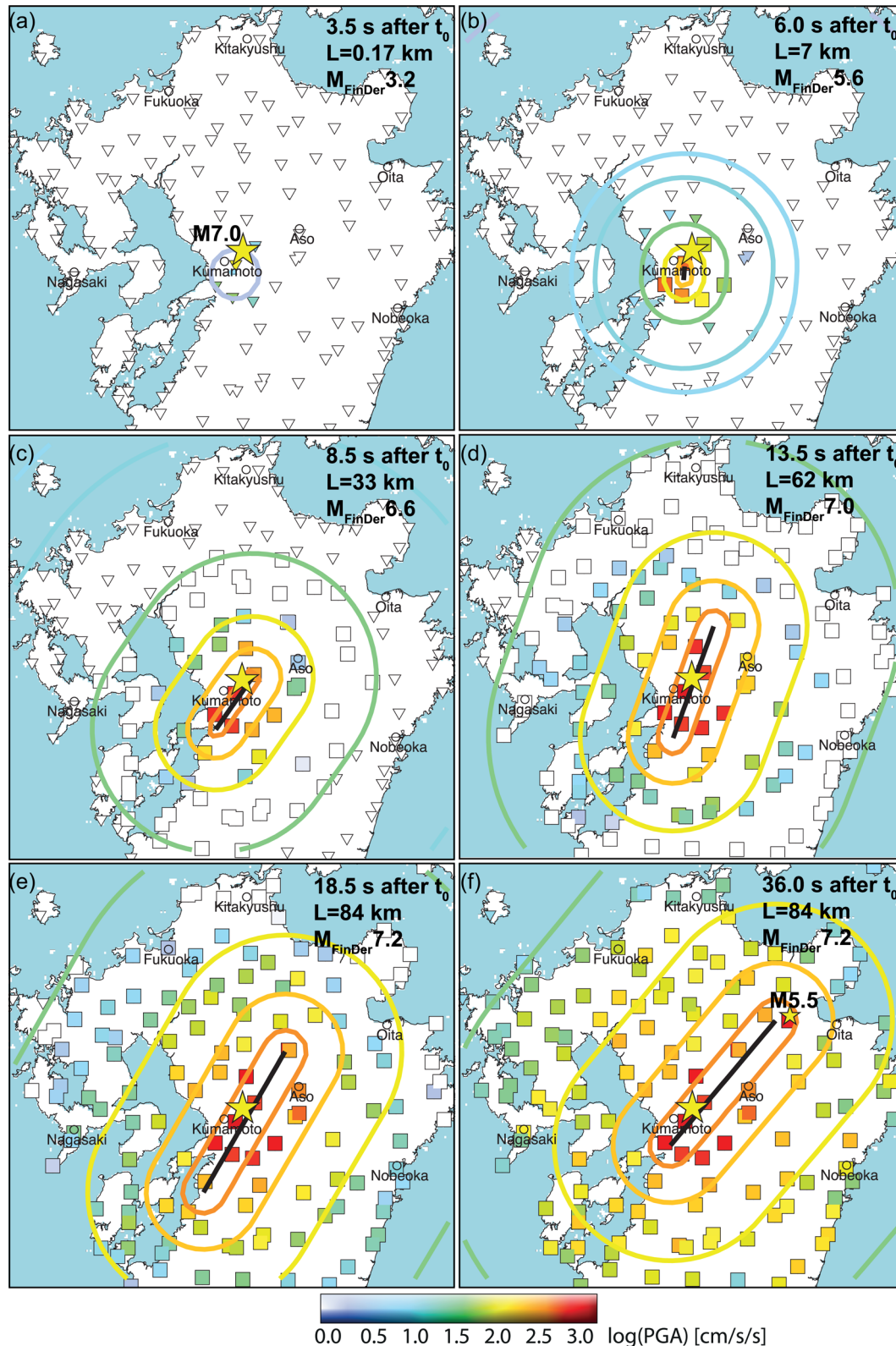


**Figure 3.** FinDer v.2 performance for the M7.0 Kumamoto earthquake simulated from waveform playback at 220 KIK-net and K-Net stations without processing and communication delays. (a)–(f) FinDer detects the quake within 3.5 s from event origin  $t_0$  and updates source parameter estimates for about 35 s; see Figs 4(a) and (b) for complete temporal evolution. Every 0.5 s, FinDer determines a line source (black line) that best matches the current PGA observations at all stations. Colour-coded contour lines show predicted PGA values for the best-matching line-source model. We use squares to mark stations that would have received a warning since the FinDer predicted PGA in any of the previous reports exceeds an assumed threshold of  $37 \text{ cm s}^{-1} \text{ s}^{-1}$  (corresponding to MMI 5, ‘moderate shaking’, green contour line); otherwise, we use inverted triangles. FinDer magnitudes,  $M_{\text{FinDer}}$ , are estimated from empirical rupture length–magnitude relations. Epicentres of the M7.0 and M5.5 events are displayed by stars, but are not used in the FinDer calculations. FinDer keeps track of the evolving fault rupture and provides warnings to places outside of the epicentral area with lead times of up to 40 s (see also Fig. 4c).

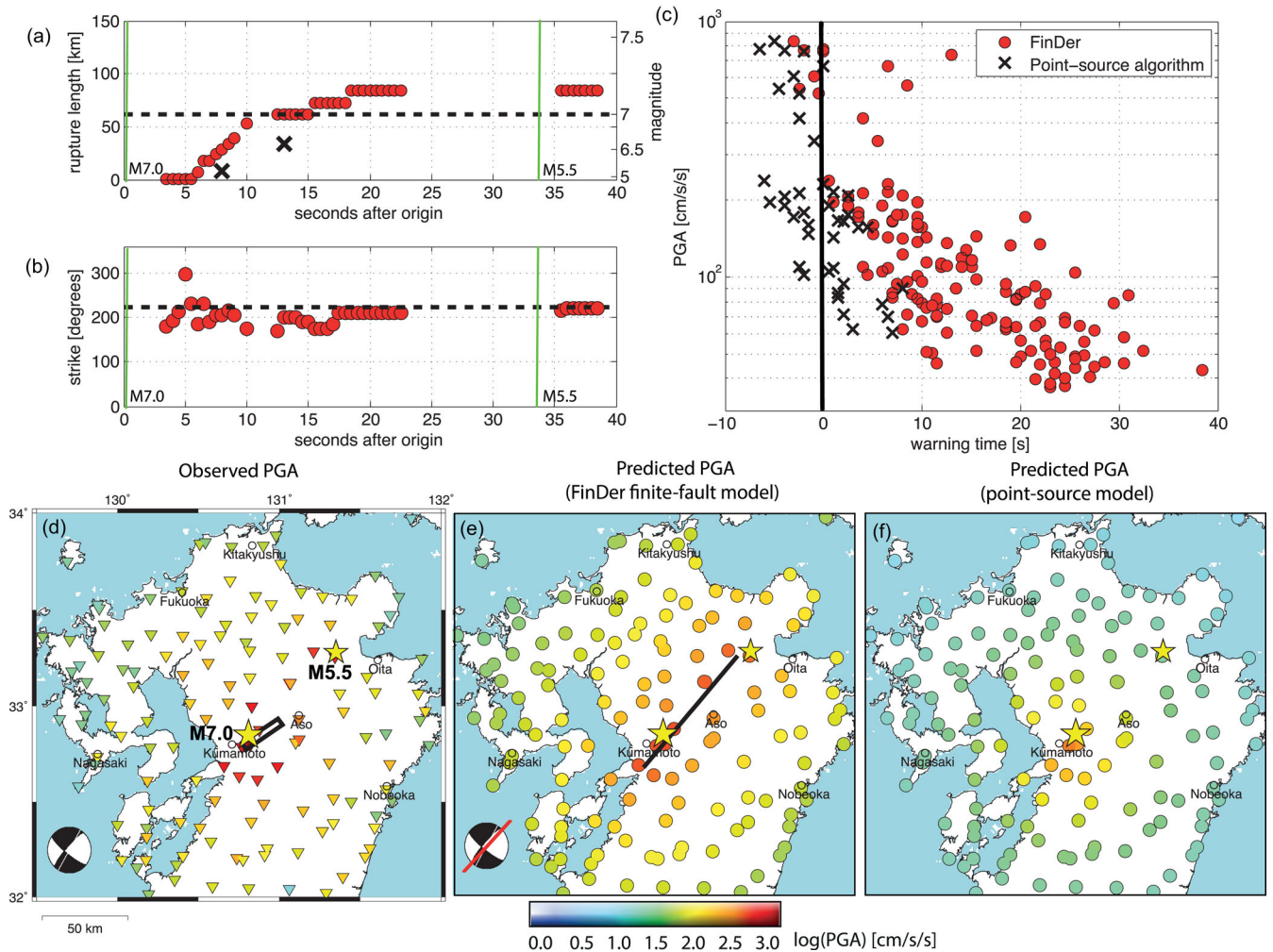


**Figure 4.** FinDer v.2 playback results for the M7.0 Kumamoto earthquake. (a) Temporal evolution of estimated rupture length and derived magnitude; updates are resumed after a short break on the occurrence of a secondary M5.5 event at 80 km distance about 30 s after the main shock. Black crosses show JMA real-time magnitude estimates (Kodera *et al.* 2016). (b) Temporal evolution of FinDer estimated rupture strike. (c) Estimated warning time at each seismic station for FinDer and a point-source algorithm. The warning time at each station is here defined as the time interval between the first prediction that ground-motions will exceed  $37 \text{ cm s}^{-1} \text{ s}^{-1}$  ( $\sim$ MMI 5 and  $\sim$ JMA 3) using GMPEs of Cua & Heaton (2009) and the actual first exceedance of this level. The occurrence of peak shaking usually occurs later so that this is the minimum warning time the system could provide, assuming zero processing delays. For the point-source algorithm, we show the actual performance of the JMA system (including delays), when GMPEs of Cua & Heaton (2009) are used. (d) Final PGA observations and NIED determined rupture plane for the M7.0 main shock. (e) PGA predicted from distances to FinDer estimated line-source (black line). (f) Predicted PGA for a point-source model using the correct catalogue hypocentre and magnitude (M7.0) using Cua & Heaton (2009). Real-time line-source models as determined by FinDer provide improved shaking forecasts compared to traditional point-source algorithms. The final FinDer model fits ground-motion observations from both the Kumamoto main shock and the smaller M5.5 earthquakes at 80 km distance.

strengths of the FinDer algorithm: by design, it provides robust ground-motion predictions rather than source characterizations. In such cases of complicated source behaviour, the ground-motion predictions remain robust and accurate even if the source characterization may not describe all the complexities of the source (see Discussion section).

The warning times that an EEW algorithm can provide depend (aside from data latency) on how quickly its ground-motion predictions exceed a critical threshold level (Meier 2017) above which end users would like to take emergency actions (e.g. Cauzzi *et al.* 2016b). Because the observed ground motions can gain intensity very rapidly, especially at sites near the epicentre, it is not a given that the predicted ground motion reaches the threshold level before the observed ground motion.

Fig. 5 shows the FinDer ground-motion prediction residuals for each station around the Kumamoto earthquake as a function of

warning time. Here, warning time is the time until the observed ground acceleration reaches  $37 \text{ cm s}^{-1} \text{ s}^{-1}$  at each individual site. For sites that have final PGA values  $< 37 \text{ cm s}^{-1} \text{ s}^{-1}$ , we use the S-phase arrival as a reference time. For all sites, the FinDer ground-motion predictions start off too low when the event is first detected and its size is initially underestimated (Fig. 3). Over the next  $\sim 10$  s, however, both the event itself and the FinDer source characterization rapidly grow towards the final size, leading to higher and more accurate ground-motion predictions. After  $\sim 10$  s, the ground-motion predictions reach a stable level that is, on average, accurate, as shown by the near-zero median prediction residual. Underpredicted ground motions are typically off by less than a factor of two from the observed ground-motion (5th percentile of log-residual distribution at  $\sim 0.3$ ). For sites with overpredicted ground motions, the residuals can be larger, with a 95th percentile of  $\sim -0.6$ , corresponding to an overprediction by a factor of 4.



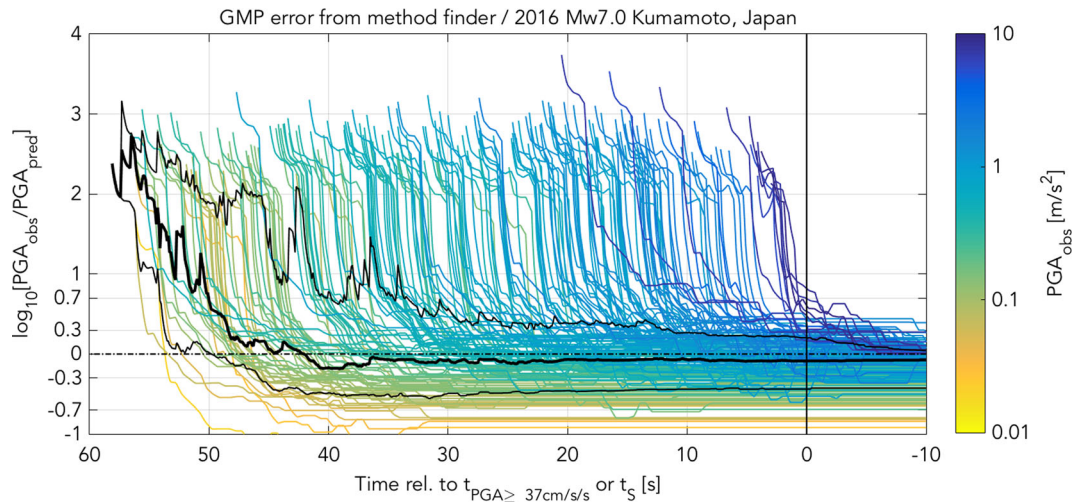


**Figure 5.** PGA prediction residuals as a function of warning time for the Kumamoto earthquake. Each line shows the evolution of the prediction for an individual site (station). Warning time is defined for each site as the time until observed accelerations exceed  $37 \text{ cm s}^{-1} \text{ s}^{-1}$  or, for sites with lower PGA, until the direct  $S$ -phase arrival. Lines are coloured by final observed peak acceleration at each site. Black lines show 5th, 50th and 95th percentiles at each point in time. The median prediction residual is close to 0. At short warning times ( $< 10 \text{ s}$ ), the 5th percentile is around 0.3 which corresponds to a PGA underprediction by a factor of  $\sim 2$ , and the 95th percentile is around  $-0.6$ , corresponding to an overprediction by a factor of  $\sim 4$ .

The residual curves in Fig. 5 show that the FinDer ground-motion predictions are fast enough to provide alerts with positive warning times for most sites. Even for sites with accelerations of  $\sim 10$  per cent  $g$  accurate ground-motion prediction levels are reached  $\geq 10 \text{ s}$  before the threshold acceleration of  $37 \text{ cm s}^{-1} \text{ s}^{-1}$  is reached at those sites. For more distant sites, with lower ground-motion amplitudes, accurate predictions become available with close to a minute of warning time. Only for the sites closest to the epicenter, it is unclear whether a warning could have been provided before the strong ground-motion starts. The size of the blind zone depends on the delays and on the selected ground-motion threshold to trigger an alert (here  $37 \text{ cm s}^{-1} \text{ s}^{-1}$ ).

In summary, FinDer would have successfully alerted all sites outside the blind zone, but may also have alerted some distant sites for which ground motions ended up being smaller than expected. Note that ground-motion overpredictions for Kumamoto have also been reported for the PLUM EEW method of Kodera *et al.* (2016).

### Example 2: M6.0 South Napa (California) earthquake

The M6.0 South Napa earthquake on 2014 August 24, 10:20:44 UTC, about 10 km south-southwest of Napa, California, caused significant local damage (Bray *et al.* 2014). From the joint inversion of seismic, Global Positioning System (GPS) and Interferometric Synthetic Aperture Radar (InSAR) data, Dreger *et al.* (2015) determine the strike of the Napa earthquake as  $155^\circ$ , which is consistent with the Global Centroid Moment Tensor (CMT) solution (Ekström *et al.* 2012) and the orientation of the West Napa fault system. The kinematic model of Dreger *et al.* (2015) suggests considerable rupture directivity towards Napa County, which agrees well with the observed ground motions and damage pattern of the strike-slip earthquake (Bray *et al.* 2014). Geological mapping showed that the South Napa earthquake was associated with an approximately 14 km long surface rupture (Bray *et al.* 2014), which coincides with the aftershock distribution and also with the empirical magnitude-rupture length relations of Wells & Coppersmith (1994).

The Californian ShakeAlert warning system in development (<http://www.shakealert.org>; Allen 2013; Böse *et al.* 2013a; Given

*et al.* 2014) detected the South Napa earthquake within 5.1 s (Grapenthin *et al.* 2014b). The initial location and magnitude errors were 3 km and 0.3 units relative to the Advanced National Seismic Networks (ANSS) catalogue. The magnitude was updated from M5.7 to M5.9 after approximately 22 s from the event origin.

In order to simulate the performance of FinDer v.2 for the M6.0 South Napa earthquake, we run a playback of the archived waveforms recorded at 74 strong-motion stations of the CISN, which are available to the ShakeAlert warning system in real time. Again, we neglect data communication and processing delays ( $\sim 1\text{--}2 \text{ s}$ ) and update estimates every half a second.

Similar to the Kumamoto earthquake, FinDer detects the South Napa earthquake within 3.5 s from the event origin, when the minimum ground-motion threshold of  $2 \text{ cm s}^{-1} \text{ s}^{-1}$  is exceeded at two stations (Fig. 6a). The magnitude is initially underestimated as  $M_{\text{FinDer}} 3.4$ , but quickly updated and reaches its final value of  $M_{\text{FinDer}} 6.0$  within 9.5 s from the event origin. The complete evolution of FinDer determined length and strike estimates over time is shown in Figs 7(a) and (b). The length and strike of the final line source are estimated as  $L = 13 \text{ km}$  and  $\Theta = 160^\circ$ , which is in excellent agreement with the kinematic source model of Dreger *et al.* (2015), as well as with the CMT solution and observed aftershock distribution. The initial FinDer line-source model (Fig. 6f) suggests a unilateral rupture towards southeastern direction, mainly caused by considerable shaking of  $> 37 \text{ cm s}^{-1} \text{ s}^{-1}$  at strong-motion station NMI operated by Northern California Seismic Network, southwest of Vallejo. The final solution, however, prefers rupture towards North-Western direction, based on a better match between the predicted (by the corresponding template) and the observed ground motions.

Although the benefit of a finite-fault detector is less pronounced in this moderate-sized event compared to the larger M7.0 Kumamoto earthquake, the predicted ground motions are improved compared to the point-source approximation (Fig. 7f). Fig. 8 shows the ground-motion prediction residuals for the South Napa earthquake. The predicted ground-motion amplitudes grow rapidly with the fault size estimate, and  $\sim 3 \text{ s}$  after event detection they reach

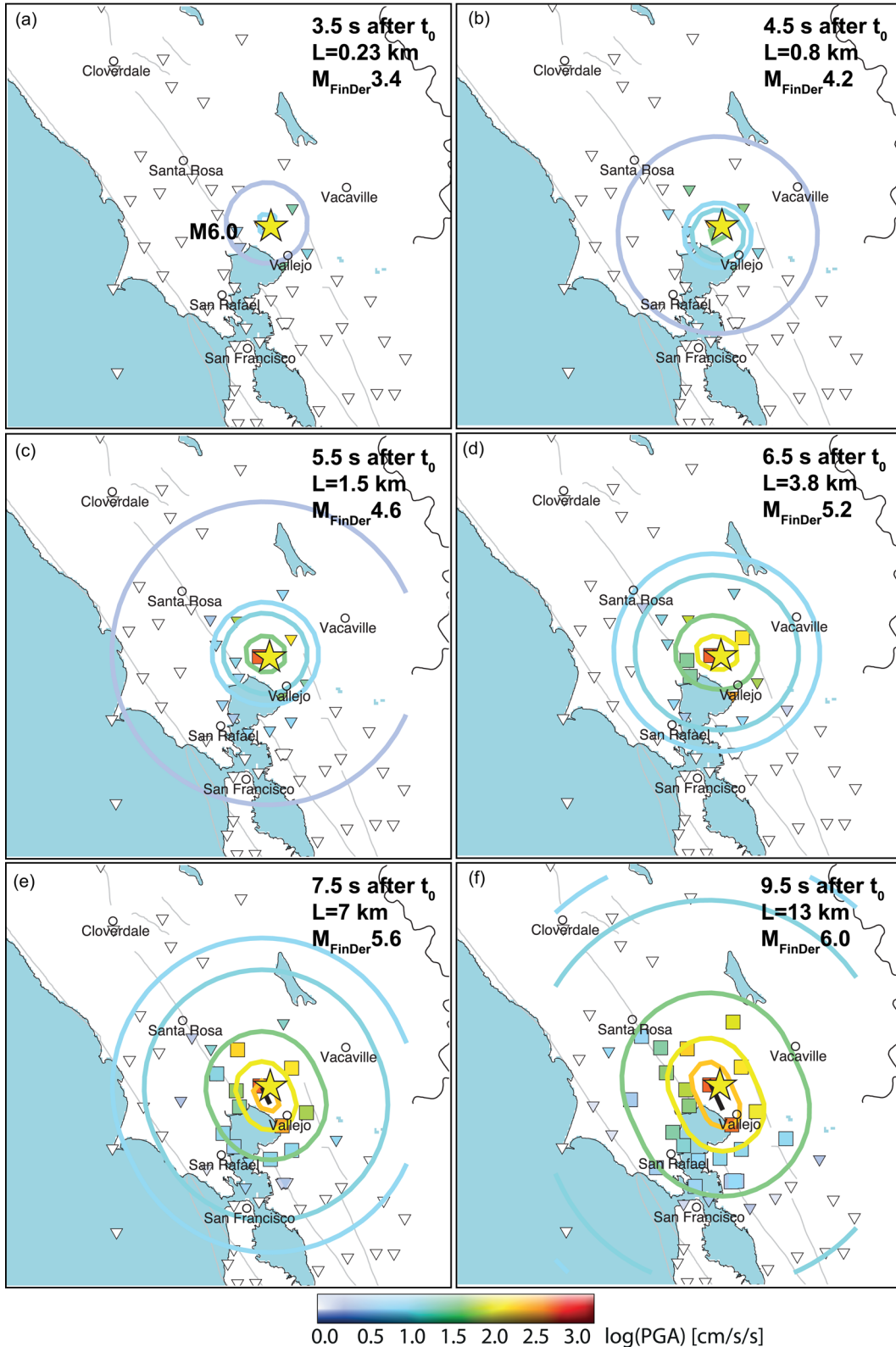


**Figure 6.** FinDer v.2 performance for the M6.0 South Napa earthquake simulated from playback of waveforms at 74 CISM strong-motion stations without processing and communication delays. Follows Fig. 3.

on average accurate prediction levels. A further increase in the estimated rupture size  $\sim 3$  s later leads to a corresponding increase in the predicted ground motions. The final ground-motion prediction overestimates the observed ground motion by a factor of 1.5

for the median (50th percentile at  $\sim 10^{0.18}$ ) and by a factor of 3.8 ( $=10^{0.58}$ ) for the 95th percentile. Warning times range from 0 to  $\sim 30$  s. Similar to the Kumamoto case, FinDer would have alerted all sites outside a small blind zone and may have alerted some

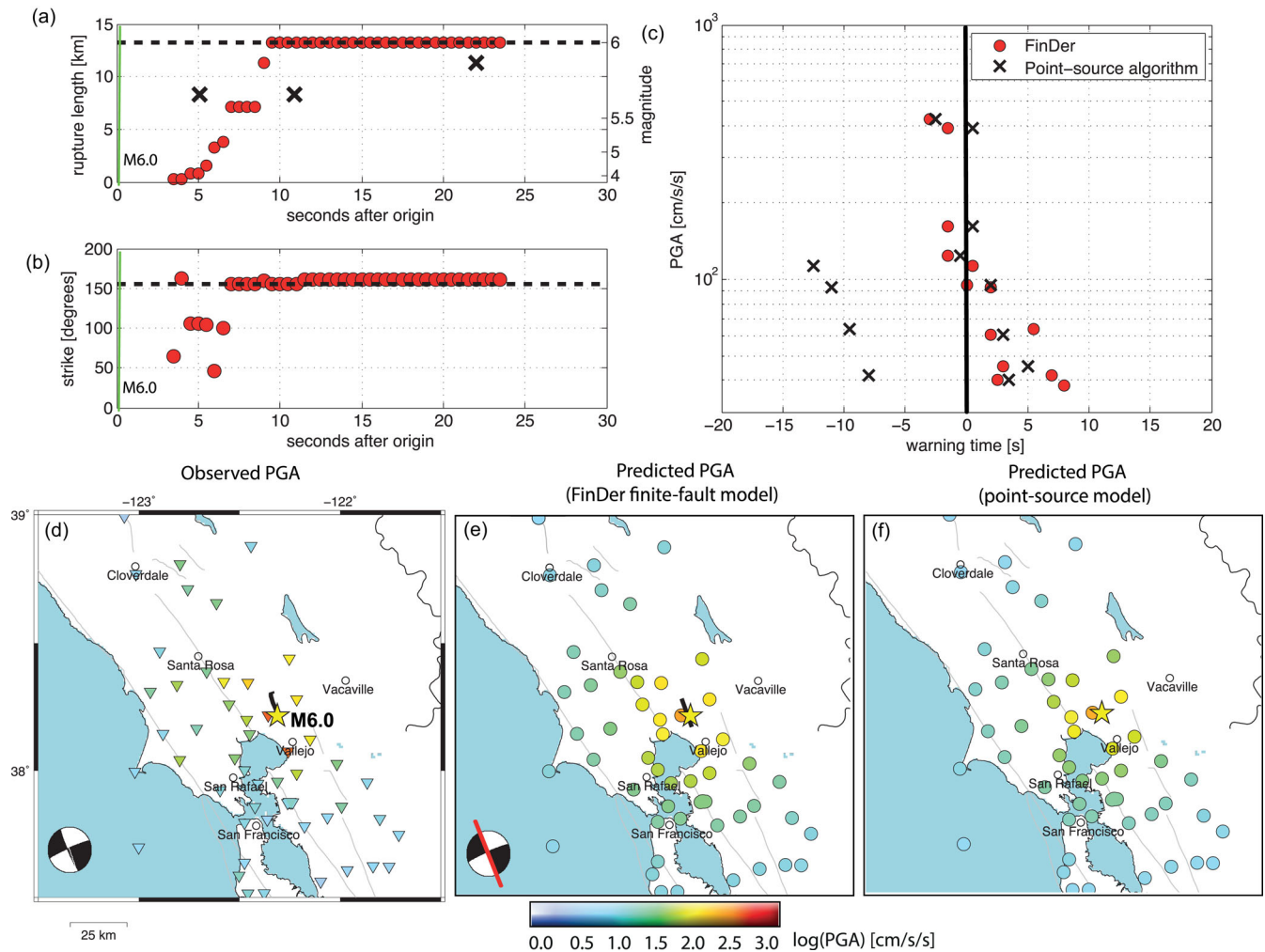


**Figure 7.** FinDer v.2 playback results for the M6.0 South Napa earthquake. Follows Fig. 4.

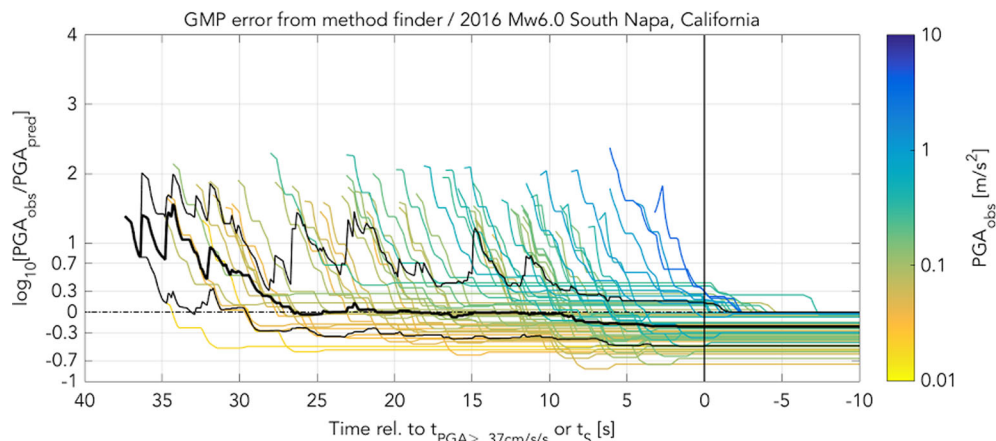


**Figure 8.** PGA prediction error as a function of warning time for the South Napa earthquake. Follows Fig. 5.

distant sites that actually experienced lower than expected ground motions.

## REAL-TIME PERFORMANCE

During an 8-month test phase from 2016 April to December, FinDer v.2 ran in real time within the Californian AQMS/Earthworm system

(Hutton *et al.* 2010; <http://www.isti.com>). Real-time waveforms from 470 CISEN strong-motion stations were processed and PGA amplitudes computed at three CISEN data centres at Caltech/US Geological Survey (USGS) Pasadena, USGS Menlo Park and UC Berkeley. During this test phase, FinDer detected and characterized 107 earthquakes with magnitudes from M2.2 to M5.1, most of them within 5–10 s from their event origin (Fig. 9).

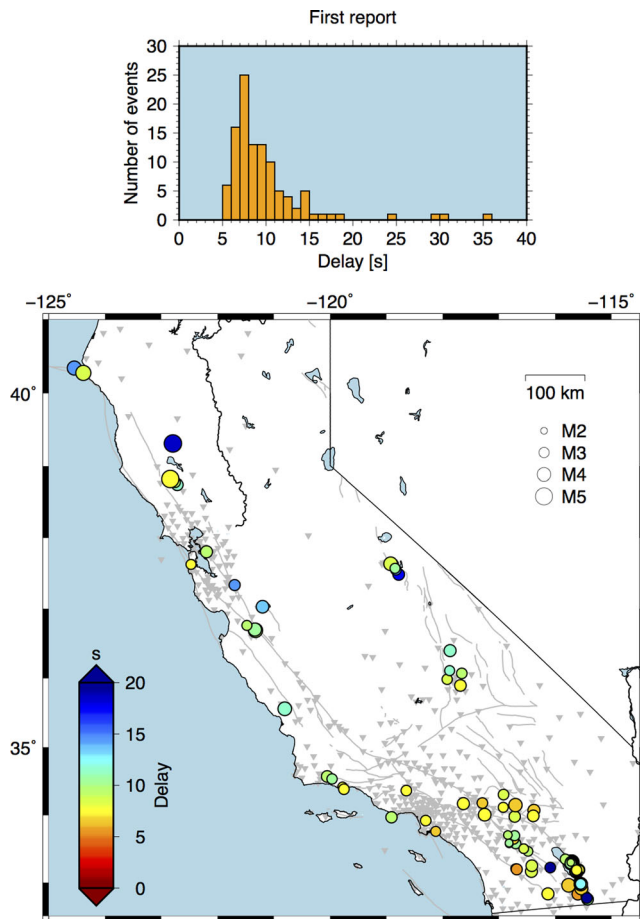


**Figure 9.** Observed delays between earthquake origin and the first FinDer v.2 alert for all 107 real-time detected events in California between 2016 April and December. Detection speed is controlled by station density, data latencies, processing and FinDer internal triggering criteria (here: at least two neighbouring stations need to report  $> 2 \text{ cm s}^{-1} \text{ s}^{-1}$ ). Most events were detected within 5–10 s from event origin.

Both the waveform-processing module for PGA computation and the FinDer code underwent several changes during the test period, which complicates the performance assessment. We can, however, provide a consistent error assessment for all detected events by using the amplitudes and timestamps that were stored by FinDer during the real-time operation, and by playing them back with the latest FinDer code and configuration. This way we can mimic the true temporal evolution of FinDer processing (with true data latencies stored in the files), while magnitude and location results may in some cases differ slightly from the real-time results (usually in the order of 0.1–0.2 mag units and up to 5 km in location).

Fig. 10 summarizes the FinDer results from first-report, 5 s afterwards, and final report in terms of both magnitude and location errors. Magnitudes tend to be slightly underestimated in the first report (on average by  $0.1 \pm 0.4$  units), and in the final report overestimated (on average by 0.2 units). Location estimates hardly change over time; errors are typically on the order of 5 km, corresponding to our current *image* and *template* spatial resolution.

As demonstrated in this paper for the M6.0 South Napa and M7.0 Kumamoto earthquakes, the FinDer-determined rupture strike for moderate and large earthquakes tends to agree well with the later determined focal mechanism and moment tensor solutions (Figs 4e

and 6e, lower left corner). This observation is not limited to strike-slip events with considerable horizontal movements, but also applies to normal- and thrust-fault events (Böse *et al.* 2012a, 2015). In the latter case, however, the FinDer line source could translate in the fault perpendicular direction by several kilometres to reach a better match with the observed ground-motion pattern resulting from fault dip.

Although high-frequency motions are less affected by rupture directivity compared to mid and long periods (Spudich & Chiou 2008), it turns out that directivity actually plays an important role in the FinDer-computed strike, especially for small earthquakes. In Fig. 11, we apply the rake-based classification algorithm for faulting style described in Shearer *et al.* (2006), to assign continuous values  $ft$  from  $-1$  to  $1$  to the earthquakes, that were real time detected by FinDer during the 8-month trial period in California; we classify all earthquakes with  $-0.25 \leq ft \leq -0.25$  as strike slip, with  $ft < -0.25$  as thrust-, and with  $ft > 0.25$  as normal-fault events.

For most events ( $2.2 \leq M \leq 5.1$ ), the FinDer-determined rupture strike and the strike of one nodal plane of the corresponding focal mechanism differ by less than  $25^\circ$  (Fig. 11). As expected, this is especially true for the strike-slip earthquakes, but also for many normal and thrust events (Fig. 12). Nevertheless, further studies are needed to confirm that the FinDer-determined strike agrees with the strike of the preferred rupture plane rather than of the auxiliary plane. We expect that this is true for the majority of events. This observation would be also consistent with earlier studies (Boatwright 2007; Seekins & Boatwright 2012) that find evidence for rupture directivity in small- to moderate-sized earthquakes ( $3.5 \geq M \geq 5.4$ ). We expect that resolving fault-plane ambiguities of small to large earthquakes within a few seconds could be extremely useful to constrain the faults along which rupture is occurring. This knowledge will have important implications for the predicted ground motions and aftershock probabilities (e.g. Böse & Heaton 2010).

## DISCUSSION

FinDer determines earthquake rupture extent from the observed level and distribution of near-source high-frequency motions. Based on a computationally highly efficient template matching methodology, FinDer determines line-source models and likelihood functions within less than 1 s and continuously updates these parameters as long as fault rupture is occurring. As demonstrated in this paper for the M7.0 Kumamoto and M6.0 South Napa earthquakes, warnings can be provided to the more remote locations, several to tens of seconds before substantial shaking at these sites initiates. A traditional point-source algorithm will probably fail to alert in these events, because shaking tends to be underestimated and warnings may not be issued when source dimensions are neglected.

There is an important conceptual difference in FinDer compared to other EEW algorithms: FinDer quantifies current fault rupture extent without predicting future rupture evolution. The algorithm is thus independent from the open question of whether or not fault rupture is deterministic and thus predictable from early waveform observations (e.g. Ellsworth & Beroza 1995; Iio 1995; Olson & Allen 2005; Rydelek & Horiuchi 2006; Colombelli *et al.* 2014). In a recent study, Meier *et al.* (2016) found that small and large earthquakes have indistinguishable waveform onsets that make it impossible to predict how large an earthquake will ultimately grow. Although for some events, FinDer v.2 could be slightly slower than traditional EEW algorithms that are optimized for small- and moderate-sized

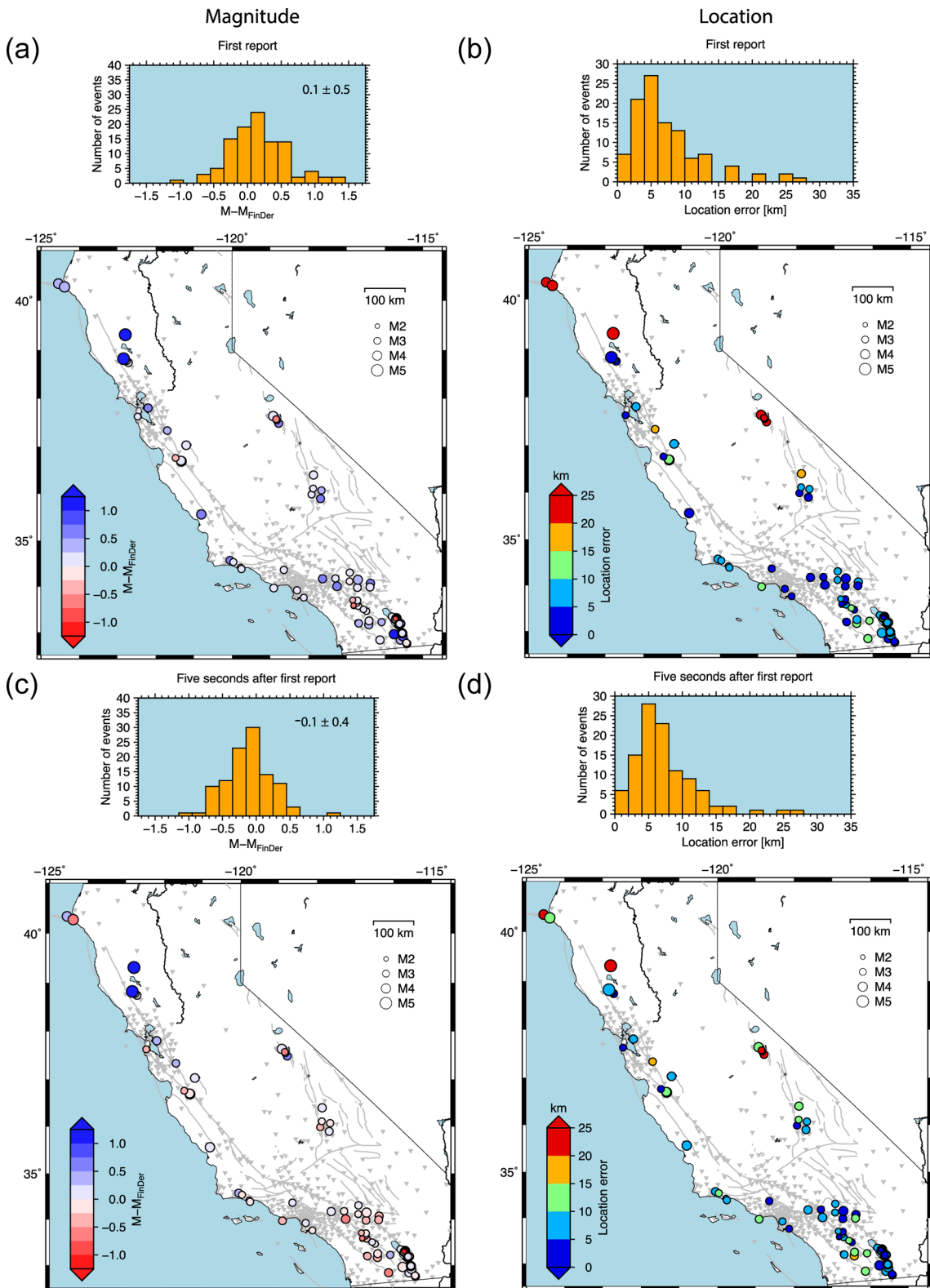


**Figure 10.** (a), (a) and (e) Magnitude and (b), (d) and (f) location errors for 107 FinDer v.2 real-time detected events in California. (a) and (b) Shown are the results of the first report, (c) and (d) 5 s later and (e) and (f) the final report. Magnitudes tend to be slightly underestimated in the first report (on average by 0.1 units), and in the final report overestimated (on average by 0.2 units). Location estimates hardly changes over time; errors are typically around 5 km, which is our current *image* and *template* spatial resolution.

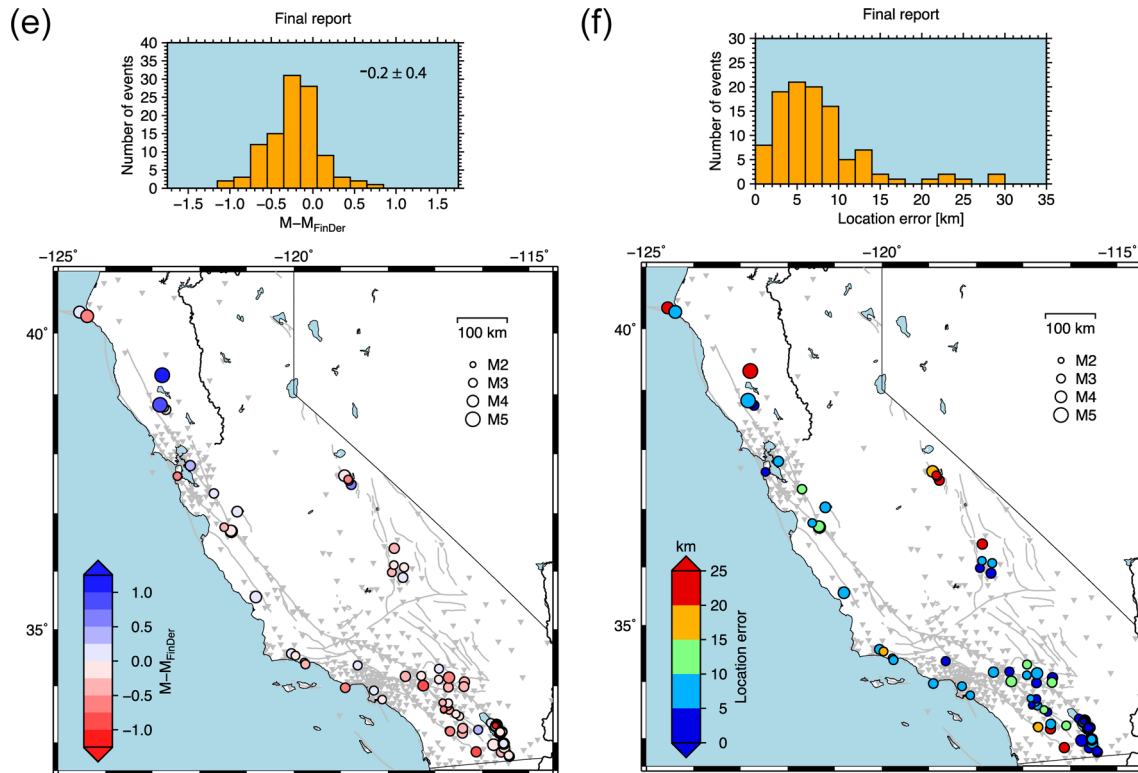
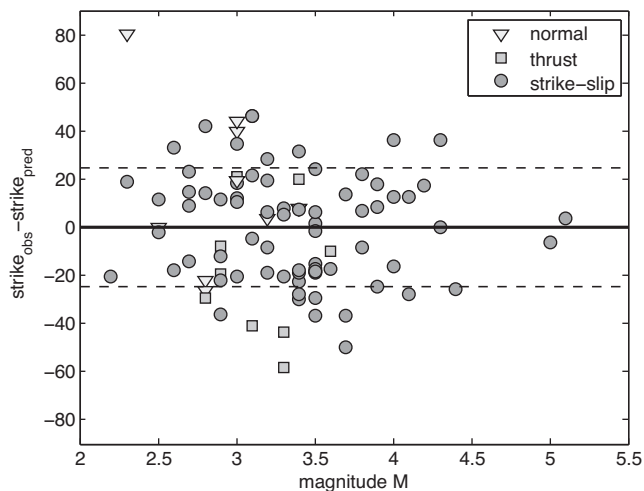


Figure 10. – Continued.



**Figure 11.** Angular difference between the FinDer-determined strike ( $\text{strike}_{\text{pred}}$ ) and the closest focal mechanism plane ( $\text{strike}_{\text{obs}}$ ) as a function of magnitude for the real-time detected earthquakes in California during the 8-month test phase. Differences are smallest for strike-slip events of larger magnitude ( $M > 3.5$ ). However, the standard deviation for all events is with  $\pm 25^\circ$  (dashed lines) small and suggests that the FinDer-determined strike could provide useful information on rupture orientation and fault recognition, including those of small earthquakes. Future studies are needed to confirm that the FinDer-determined strike agrees with the strike of the preferred rupture plane.

earthquakes, it provides the necessary tool to characterize earthquakes that start small, but grow larger over time.

The advantage of a finite-fault detector like FinDer is most apparent for EEW in a major event, such as the M7.0 Kumamoto main

shock. Knowing rupture extent within seconds, however, can also help to quickly identify causative faults and predict future aftershock activity in the smaller magnitude earthquakes. FinDer output might be also useful for rapid response tools, such as ShakeMap (Wald *et al.* 1999). For example in the South Napa earthquake, the USGS released a first ShakeMap within a few minutes from the event origin. However, it took several days for the rupture dimensions to be assessed, mainly from the aftershock distribution and field surveys, and added to ShakeMap (Wald, private communication, 2016). FinDer could provide within seconds initial constraints on rupture extent and seismic ground motions at sites lacking station observations, until more accurate and detailed finite-fault models become available.

Modern seismic networks, such as in California or Japan, have average data latencies of 1 s and less. FinDer can accommodate stations with notoriously large latencies, which are known because of the time stamps. Real-time runs of FinDer in California, Switzerland, Chile, and Nicaragua, have shown that the algorithm does not produce inaccurate source descriptions due to data latencies, but is, of course, slowed down, like any other EEW algorithm.

FinDer v.2 extends the original FinDer algorithm (Böse *et al.* 2012a) by providing a consistent modeling approach and uncertainty assessment for small and large earthquakes. This is possible, because FinDer v.2 uses a sequence of ground-motion thresholds for near-far source classification rather a single large value (e.g.  $70 \text{ cm s}^{-1}$ ) that was used in the original algorithm. While rupture dimensions are less critical for predicting the seismic ground motions in small and moderate earthquakes, allowing for the fact that large earthquakes may start as small events is fundamentally important. Unlike traditional approaches in which small and large earthquakes are treated separately, our finite-fault modeling approach (for small and large earthquakes) allows for a coherent and robust



**Figure 12.** Comparison of FinDer-determined rupture strike (red line) and focal mechanisms/moment tensor solutions for the real-time detected earthquakes ( $2.2 \leq M \leq 5.1$ ) shown in Fig. 11. The size of the beachballs scales with magnitude. We apply a rake-based classification of faulting style (Shearer *et al.* 2006) that produces output values  $ft$  from  $-1$  to  $1$ . For most events, the FinDer-determined rupture strike and the strike of one nodal plane of the corresponding focal mechanism agree to within  $\pm 25^\circ$ . Errors are smallest for the strike slip ( $-0.25 \leq ft \leq -0.25$ ) earthquakes, but strike estimates for many normal ( $ft < -0.25$ ) and thrust ( $ft > 0.25$ ) events are reasonable.

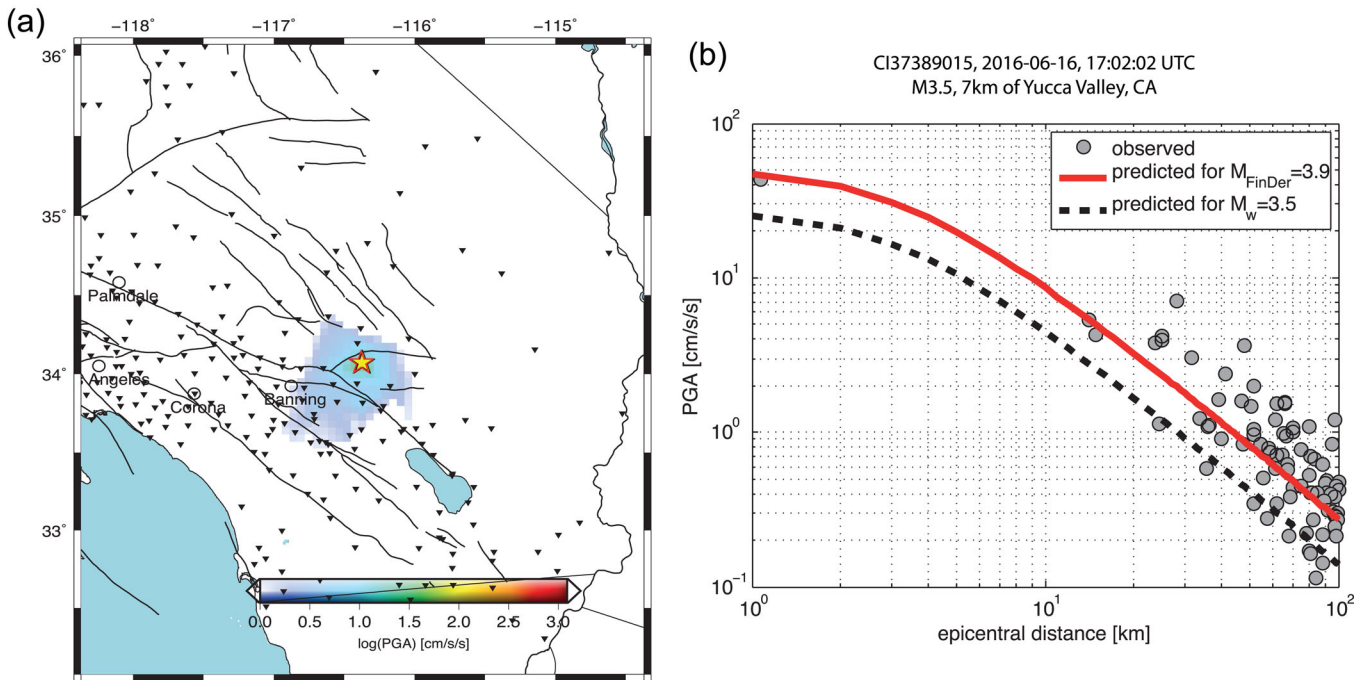


**Figure 13.** Comparison of observed and predicted peak ground-acceleration (PGA) for the 2016 M3.5 Yucca Valley, California, earthquake. (a) Interpolated observed PGA at CISM strong-motion stations; the FinDer determined epicentre (yellow star) agrees well with the ANSS solution (red star). The FinDer determined magnitude is with  $M_{\text{FinDer}} = 3.9$  0.4 mag units higher than in the ANSS catalogue. (b) Using the larger FinDer magnitude in the GMPEs (here Cua & Heaton, 2009) gives a significantly better match with the observed PGA values compared to the smaller M3.5 catalogue magnitude. FinDer is optimized to characterize seismic ground motions rather than the earthquake source—as is needed for EEW.  $M_{\text{FinDer}}$  can be interpreted as a scaling factor that tunes the fit of a given GMPE (used for template generation) and the observed near-source high-frequency motions.

interpretation of output parameters and uncertainty estimates for EEW, without abrupt changes during rupture growth.

Because FinDer updates peak amplitudes and line-source estimates as long as these values increase, it is possible to characterize earthquakes that start shortly after a foreshock. An extreme example is the 2010 M7.2 El-Mayor Cucupah earthquake in Northern Mexico which began as a smaller  $\sim$ M6 normal faulting quake and was followed  $\sim$ 15 s later by the normal/strike-slip faulting main shock (Wei *et al.* 2011; Böse *et al.* 2015). EEW algorithms that are based only on the first few seconds of waveforms will likely fail to characterize events like El-Mayor.

Unlike other EEW algorithms that determine event parameters, such as magnitudes, from values averaged over a subset of independent station estimates (e.g. Allen 2007; Kuyuk *et al.* 2014), FinDer computes true network solutions, including null data from PGA observations at stations far off from the detected event. This holistic view allows FinDer to capture event-specific features, such as effects of rupture directivity or seismic radiation, which may remain hidden otherwise.

The FinDer-determined line-source models are optimized to match the observed high-frequency ground-motion amplitudes close to the earthquake epicentre. If an earthquake emits unusually large amounts of high-frequency motions, for instance due to a high stress drop, FinDer prefers a template with a larger magnitude compared to the earthquake catalogue. This implies that the FinDer magnitude  $M_{\text{FinDer}}$  is a tuning factor to scale the ground-motion kernels (that is the *templates* calculated from a GMPE) to match the current PGA observations (the *image*).

In Fig. 13, we show the example of the 2016 M3.5 Yucca Valley earthquake: for the GMPEs (here Cua & Heaton 2009), the 0.4 units higher FinDer magnitude,  $M_{\text{FinDer}} = 3.9$ , achieves a clearly better fit

with the observed PGA at the CISM stations than the smaller ANSS catalogue magnitude M3.5. Thus, FinDer is optimized to characterize seismic high-frequency motions rather than the earthquake source (i.e. is usually closer to  $M_L$  rather than  $M_w$ ; for the Yucca Valley earthquake  $M_L$  is determined as 3.7), which is clearly advantageous for EEW, in which rapid shaking and damage assessments are needed rather than accurate source descriptions.

EEW algorithms are usually triggered by seismic ( $P$ -)phase detections from traditional phase pickers (e.g. Küperkoch *et al.* 2011); phase arrival times at multiple stations are then used to infer earthquake locations. Due to the strict time constraints in EEW, the initial location estimates are usually based on very few ( $\sim$ 4–6) phase picks, which can lead to erroneous location estimates in the case of incorrectly picked or labeled phases. FinDer, on the other hand, continually monitors PGA across the entire seismic network. If there are at least two stations with PGAs above the minimum threshold, the ground-motion pattern is compared with the theoretical templates calculated from the GMPEs. FinDer processing starts as soon as there is a high correlation between the observed and the theoretical ground motions. This means that a warning is given only if there is a coherent ground-motion pattern across several stations. This combined approach of earthquake location and determination of source strength makes FinDer robust enough to allow its application to noisy environments, including low-cost sensors, as demonstrated recently in a smartphone network deployed in Chile (Brooks *et al.* 2016; Böse *et al.* 2016b).

A major challenge for seismic real-time systems, such as for EEW, is the risk of being accidentally triggered by a teleseismic event that is mistaken for a local earthquake. Since teleseisms, however, usually cause long-period motions, it is unlikely that a high-frequency approach like FinDer will accidentally trigger.



The initial estimates of FinDer (and FinDer v.2) magnitudes, in particular for the smaller and moderate-sized (<M6.0) earthquakes, often tend to be too small, mainly because we assume that the presently observed PGA amplitudes have reached their maximum values at the near-source stations when template matching is applied. Peak shaking at these sites, however, is typically reached within the *S*-wave phases. In the initial estimates, however, some stations will have seen the *P*-wave only. We expect that a robust *P*-*S*-wave discriminator and upscaling of *P*-wave amplitudes to (*S*-wave) PGA, similar to the Pd-PGV relations by Wu *et al.* (2007), will accelerate the convergence of the FinDer estimated magnitudes towards the final solutions. As an additional enhancement, we plan to consider the impact of site effects, particularly near the earthquake rupture.

## CONCLUSIONS

We have developed a modeling approach that is suitable for real-time characterization of finite-fault rupture extent in both small and very large earthquakes. The approach is based on the levels and distributions of seismic high-frequency motions that are controlled mainly by the distance to the rupturing fault. The algorithm uses spatial template matching to determine the position, length and strike of an assumed line source, as well as the corresponding misfit and likelihood functions. The playback of recorded waveforms of the 2016 M7.0 Kumamoto and the 2014 M6.0 South Napa earthquakes in this paper demonstrates that both shaking forecasts and warning times are improved relative to a traditional point-source algorithm. During an 8-month test phase, in which we ran the algorithm in real time within the Californian AQMS/Earthworm system of the CISN, FinDer detected around 100 earthquakes, most of them within 5–10 s from their event origin, with errors of  $\pm 0.4$  (standard deviation) magnitude units and about 5 km in location. Initial magnitudes tended to be slightly underestimated, and final magnitudes slightly overestimated, which is mainly due to the uncertainties of the GMPEs used for template generation in FinDer. In addition to the described real-time tests in California, FinDer is currently being real time tested in Chile, Switzerland, and Central America. Performance results will be described in forthcoming publications.

## DATA AND RESOURCES

Seismic waveform and catalogue data used in this study were downloaded from CISN ([www.cisn.org](http://www.cisn.org)) and NIED (<http://www.bosai.go.jp/e/>). Plots were generated with GMT version 5.2 (Wessel *et al.* 2013) and Mathworks Matlab. The W-Phase moment tensor Solution for the Kumamoto main shock was obtained from the NEIC/USGS (<https://earthquake.usgs.gov/>). The Global CMT for the South Napa earthquake was obtained from <http://www.globalcmt.org/CMTsearch.html>. All data was last accessed in 2017 March.

## ACKNOWLEDGEMENTS

We would like to thank the following persons for scientific discussions and support of this work: S. Minson, J. Andrews, F. Massin, S. Carrasco, S. Guiwits, E. Cochran, S. Wiemer, B. Brooks, E. Hauks-son, R. Bhadha, S. Heimers, P. Kaestli, F. Euchner, J. Becker, C. Cauzzi, M. Black, Y. Behr, D. Given and J. Langbein. We are also grateful for USGS internal reviews by Ruth Harris and Benjamin

Brooks. We would like to thank A. Oth, an anonymous reviewer, and editor M. Mai for their thorough reviews.

## REFERENCES

- Allen, R.M., 2007. The AlarmS earthquake early warning methodology and its application across California, in *Earthquake Early Warning Systems*, eds Gasparini, P., Manfredi, G. & Zschau, J., pp. 21–44, Springer.
- Allen, R., 2013. Seconds count, *Nature*, **502**, 29–31.
- Behr, Y. *et al.*, 2016. The virtual seismologist in SeisComp3: a new implementation strategy for earthquake early warning algorithms, *Seismol. Res. Lett.*, **87**(2A), doi:10.1785/0220150235.
- Behr, Y., Clinton, J., Kaestli, P., Cauzzi, C., Racine, R. & Meier, M.-A., 2015. Anatomy of an earthquake early warning (EEW) alert: predicting time delays for an end-to-end EEW system, *Seismol. Res. Lett.* **86**, 830–840.
- Boatwright, J., 2007. The persistence of directivity in small earthquakes, *Bull. seism. Soc. Am.* **97**(6), 1850–1861.
- Bock, Y., Melgar, D. & Crowell, B.W. 2011. Real-time strong-motion broadband displacements from collocated GPS and accelerometers, *Bull. seism. Soc. Am.* **101**(6), 2904–2925.
- Bommer, J.J. & Akkar, S., 2012. Consistent source-to-site distance metrics in ground motion prediction equations and seismic source models for PSHA, *Earthq. Spectra*, **28**(1), 1–15.
- Böse, M., Behr, Y., Heaton, T.H. & Clinton, J. 2016a. From single-station prediction to finite-fault detection: the large spectrum of EEW algorithms and the question of how to combine them, in *Proceedings of ECGS and ESC/AEE Joint Workshop: Earthquake and Induced Multi-Risk Early Warning and Rapid Response*, Cahiers Bleus of ECGS, Vol. 31, eds Oth, A. & Parolai, S. Luxembourg, 2015 November 18–20.
- Böse, M. *et al.*, 2016b. Smartphone-network for Earthquake and Tsunami Early Warning in Chile, in *35rd General Assembly of the European Seismological Commission (GA ESC)*, eds Oth, A. & Parolai, S. 2016 September 4–11, Trieste, Italy.
- Böse, M., Felizardo, C. & Heaton, T.H., 2015. Finite-Fault Rupture Detector (FinDer): going real-time in Californian ShakeAlert warning system, *Seismol. Res. Lett.*, **86**(6), 1692–1704.
- Böse, M., Graves, R., Gill, D., Callaghan, S. & Maechling, P., 2014. CyberShake-derived ground-motion prediction models for the Los Angeles region with application to EEW, *Geophys. J. Int.*, **198**(3), 1438–1457.
- Böse, M. & Heaton, T.H. 2010. Probabilistic prediction of rupture length, slip and seismic ground motions for an ongoing rupture: implications for Early Warning for large earthquakes, *Geophys. J. Int.*, **183**(2), 1014–1030.
- Böse, M. *et al.*, 2013a. CISN ShakeAlert—an Earthquake Early Warning demonstration system for California, in *Early Warning for Geological Disasters - Scientific Methods and Current Practice*, eds Wenzel, F. & Zschau, J. Springer Berlin Heidelberg, New York, 49–69, ISBN: 978-3-642-12232-3.
- Böse, M., Heaton, T. & Hudnut, K., 2013b. *Combining Real-Time Seismic and GPS Data for Earthquake Early Warning*, AGU (American Geophysical Union) 2013 Fall Meeting, #G51B-05.
- Böse, M., Heaton, T.H. & Hauks-son, E. 2012a. Real-time Finite Fault Rupture Detector (FinDer) for large earthquakes, *Geophys. J. Int.*, **191**(2), 803–812.
- Böse, M., Heaton, T. & Hauks-son, E., 2012b. Rapid estimation of earthquake source and ground-motion parameters for earthquake early warning using data from single three-component broadband or strong-motion sensor, *Bull. seism. Soc. Am.*, **102**(2), 738–750.
- Böse, M., Wenzel, F. & Erdik, M., 2008. PreSEIS: a neural network based approach to Earthquake Early Warning for finite faults, *Bull. seism. Soc. Am.*, **98**(1), 366–382.
- Bray, J., Cohen-Waeber, J., Dawson, T., Kishida, T. & Sitar, N., 2014. Geotechnical engineering reconnaissance of the August 24, 2014 M6 South Napa earthquake, GEER Association Rep. No. GEER-037, in collaboration with the California Geological Survey, Pacific Earthquake Engineering Research Center, and U.S. Geological Survey, with support from NSF. ver. 1, 402 pp.

- Brooks, B.A. *et al.*, 2016. *Smartphone-Based Earthquake Early Warning in Chile*, UNAVCO Science Workshop.
- Cauzzi, C., Behr, Y., Le Guenan, T., Douglas, J., Auclair, S., Woessner, J., Clinton, J. & Wiemer, S., 2016a. Earthquake early warning and operational earthquake forecasting as real-time hazard information to mitigate seismic risk at nuclear facilities, *Bull. Earthq. Eng.*, **14**, 2495–2512.
- Cauzzi, C., Gasparini, P., Wiemer, S. & Zschau, J., 2016b. Preface to the special issue ‘Strategic applications of real-time risk mitigation strategies and tools: case studies and lessons learned in REAKT’, *Bull. Earthquake Eng.*, **14**, 2437–2439.
- Colombelli, S., Zollo, A., Festa, G. & Picozzi, M., 2014. Evidence for a difference in rupture initiation between small and large earthquakes. *Nat. Commun.*, **5**, 3958, doi:10.1038/ncomms4958.
- Cormen, T.H., Leiserson, C.E., Rivest, R.L. & Stein, C., 2009. *Introduction to Algorithms*, 3rd edn, The MIT Press.
- Crowell, B.W. *et al.*, 2016. Demonstration of the Cascadia G-FAST geodetic earthquake Early Warning System for the Nisqually, Washington, Earthquake, *Seismol. Res. Lett.*, **87**(3), doi:10.1785/0220150255.
- Cua, G.B. & Heaton, T.H., 2009. Characterizing average properties of southern California ground motion amplitudes and envelopes, Earthquake Engineering Research Laboratory, Pasadena, CA. Available at: <http://resolver.caltech.edu/CaltechEERL:EERL-2009-05>, last accessed June 2017.
- Cua & G. (2005). Creating the Virtual Seismologist: developments in ground motion characterization and seismic early warning. *PhD thesis*, California Institute of Technology, Pasadena, CA.
- Dreger, D.S., Huang, M.-H., Rodgers, A., Taira, T. & Wooddell, K., 2015. Kinematic finite-source model for the 24 August 2014 South Napa, California, earthquake from joint inversion of seismic, GPS, and InSAR data, *Seismol. Res. Lett.*, **86**(2A), doi:10.1785/0220140244.
- Ekström, G., Nettles, M. & Dziewonski, A.M., 2012. The global CMT project 2004–2010: centroid-moment tensors for 13,017 earthquakes, *Phys. Earth planet. Inter.*, **200–201**, 1–9.
- Ellsworth, W.L. & Beroza, G.C., 1995. Seismic evidence for an earthquake nucleation phase, *Science*, **268**(5212), 851–855.
- Given, D.D., Cochran, E.S., Heaton, T.H., Hauksson, E., Allen, R., Hellweg, P., Vidale, J. & Bodin, P., 2014. Technical implementation plan for the ShakeAlert production system—an Earthquake Early Warning system for the West Coast of the United States. Open-File Report, U.S. Geol. Surv. 2014–1097, doi:10.3133/off20141097.
- Goda, K. *et al.*, 2016. The 2016 Kumamoto Earthquakes: cascading geological hazards and compounding risks, *Front. Built Environ.*, **2**, 19, doi:10.3389/fbuil.2016.00019.
- Gonzales, R.C., Woods, R.F. & Eddins, S.L., 2004. *Digital Image Processing using MATLAB*, Pearson Prentice Hall, Upper Saddle River, NJ.
- Grapenthin, R., Johanson, I.A. & Allen, R.M., 2014a. Operational real-time GPS-enhanced earthquake early warning, *J. geophys. Res.*, **119**, 7944–7965.
- Grapenthin, R., Johanson, I.A. & Allen, R.M., 2014b. The 2014 Mw6.0 Napa earthquake, California: observations from real-time GPS-enhanced earthquake early warning, *Geophys. Res. Lett.*, **41**, 8269–8276.
- Heaton, T.H., 1985. A model for a seismic computerized alert network, *Science*, **228**, 987–990.
- Hoshiaba, M., 2017. Triggered earthquake during the 2016 Kumamoto earthquake (Mw7.0): importance of real-time shake monitoring for earthquake early warning, in *2017 Annual Meeting, Seismol. Soc. Am.*, 2017 April 18–20, Denver, CO.
- Hoshiaba, M. & Aoki, S., 2015. Numerical shake prediction for Earthquake Early Warning: data assimilation, real-time shake mapping, and simulation of wave propagation, *Bull. seism. Soc. Am.*, **105**(3), 1324–1338.
- Hoshiaba, M., Kamigaichi, O., Saito, M., Tsukada, S. & Hamada, N., 2008. Earthquake early warning starts nationwide in Japan, *EOS Trans. Am. geophys. Un.*, **89**, 73–74.
- Hutton, L.K., Woessner, J. & Hauksson, E., 2010. Seventy-seven years (1932–2009) of earthquake monitoring in southern California, *Bull. seism. Soc. Am.*, **100**(2), 423–446.
- Iio, Y., 1995. Observations of the slow initial phase generated by microearthquake nucleation and propagation, *J. geophys. Res.*, **100**(B8), 15333–15349.
- Kanamori, H., 2005. Real-time seismology and earthquake damage mitigation, *Annu. Rev. Earth planet. Sci.*, **33**, 195–214.
- Kodera, Y., Saitou, J., Hayashimoto, N., Adachi, S., Morimoto, M., Nishimae, Y. & Hoshiaba, M., 2016. Earthquake early warning for the 2016 Kumamoto earthquake: performance evaluation of the current system and the next-generation methods of the Japan Meteorological Agency, *Earth Planets Space*, **68**(1), 202, doi:10.1186/s40623-016-0567-1.
- Küperkok, L., Meier, T. & Diehl, T., 2011. Automated event and phase identification, doi:10.2312/GFZ.NMSOP-2\_ch16
- Kuyuk, S., Allen, R.M., Brown, H., Hellweg, M., Henson, I. & Neuhauser, D., 2014. Designing a network-based earthquake Early Warning Algorithm for California: ElarmS-2, *Bull. seism. Soc. Am.*, **104**(1), 162–173.
- Meier, M.-A., Heaton, T. & Clinton, J. (2015). The Gutenberg algorithm: evolutionary Bayesian magnitude estimates for Earthquake Early Warning with a filter bank, *Bull. seism. Soc. Am.*, **105**(5), 2774–2786.
- Meier, M.-A., Heaton, T. & Clinton, J. 2016. Evidence for universal earthquake rupture initiation behavior, *Geophys. Res. Lett.*, **43**, 7991–7996.
- Meier, M.-A., 2017. How ‘good’ are real-time ground motion predictions from Earthquake Early Warning systems?, *J. geophys. Res.*, **122**, doi:10.1002/2017JB014025.
- Melgar, D. *et al.*, (2015). Earthquake magnitude calculation without saturation from the scaling of peak ground displacement, *Geophys. Res. Lett.*, **42**, 5197–5205.
- Minson, S.E., Murray, J.R., Langbein, J.O. & Gomberg, J.S., 2014. Real-time inversion for finite-fault slip models and rupture geometry based on high-rate GPS data, *J. geophys. Res.*, **119**, 3201–3231.
- Nakamura, T. & Aoi, E., 2017. Source location and mechanism analysis of an earthquake triggered by the 2016 Kumamoto, southwestern Japan, earthquake, *Earth Planets Space*, **69**, 6, doi:10.1186/s40623-016-0588-9.
- Olson, E.L. & Allen, R.M., 2005. The deterministic nature of earthquake rupture, *Nature*, **438**(7065), 212–215.
- Oth, A., Bindi, D., Parolai, S. & Di Giacomo, D. 2010. Earthquake scaling characteristics and the scale-(in)dependence of seismic energy-to-moment ratio: insights from KiK-net data in Japan, *Geophys. Res. Lett.*, **37**(19), L19304, doi:10.1029/2010GL044572.
- Rydelek, P. & Horiuchi, S. 2006. Earth science: is earthquake rupture deterministic? *Nature*, **442**(7100), E5–E6.
- Satriano, C., Elia, L., Martino, C., Lancieri, M., Zollo, A. & Iannaccone, G. 2011. PRESTo, the earthquake early warning system for Southern Italy: concepts, capabilities and future perspectives, *Soil Dyn. Earthq. Eng.*, **31**(2), 137–153.
- Seekins, L.C. & Boatwright, J. 2012. Rupture directivity of moderate earthquakes in Northern California, *Bull. seism. Soc. Am.*, **100**(3), 1107–1119.
- Shearer, P.M., Prieto, G.A. & Hauksson, E. 2006. Comprehensive analysis of earthquake source spectra in southern California, *J. geophys. Res.*, **111**, B06303, doi:10.1029/2005JB003937.
- Spudich, P. & Chiou, B.S.J. 2008. Directivity in NGA Earthquake ground motions: analysis using isochrone theory, *Earthq. Spectra*, **24**(1), 279–298.
- Wald, D., Quitoriano, V., Heaton, T., Kanamori, H., Scrivner, C. & Worden, C. 1999. TriNet ShakeMaps: rapid generation of instrumental ground motion and intensity maps for earthquakes in southern California, *Earthq. Spectra*, **15**, 537–556.
- Wei, S. *et al.*, 2011. Superficial simplicity of the 2010 El Mayor-Cucapah earthquake of Baja California in Mexico, *Nat. Geosci.*, doi:10.1038/ngeo1213.
- Wells, D.L. & Coppersmith, K.J., 1994. New empirical relationships among magnitude, rupture length, rupture width, rupture area, and surface displacement, *Bull. seism. Soc. Am.*, **84**, 974–1002.
- Wessel, P., Smith, W.H.F., Scharroo, R., Luis, J.F. & Wobbe, F. 2013. Generic mapping tools: improved version released, *EOS Trans. Am. geophys. Un.*, **94**, 409–410.
- Wu, Y.-M., Kanamori, H., Allen, R.M. & Hauksson, E. 2007. Determination of earthquake early warning parameters,  $\tau_c$  and  $P_d$ , for southern California, *Geophys. J. Int.*, **170**, 711–717.

- Yagi, Y., Okuwaki, R., Enescu, B., Kasahara, A., Miyakawa, A. & Otsubo, M. 2016. Rupture process of the 2016 Kumamoto earthquake in relation to the thermal structure around Aso volcano, *Earth Planets Space*, **68**(118), doi:10.1186/s40623-016-0492-3.
- Yamada, M., Heaton, T. & Beck, J. 2007. Real-time estimation of fault rupture extent using near-source versus far-source classification, *Bull. seism. Soc. Am.*, **97**(6), 1890–1910.
- Yano, T.E. & Matsubara, M. 2016. The significance of seismicity after the 2016 Kumamoto Earthquake sequence, in *2016 Japan Geoscience Union Meeting (MIS34-P05)*.
- Zollo, A., Amoroso, O., Lancieri, M., Wu, Y.-M. & Kanamori, H., 2010. A threshold-based earthquake early warning using dense accelerometer networks, *Geophys. J. Int.*, **183**, 963–974.